

## Highlights

### **Multi-step vertical coupling via gravity waves from the lower to the upper atmosphere**

Erich Becker, Sharon L. Vadas, Xinzhao Chu

- Multi-step vertical coupling (MSVC) from primary to high-order gravity waves (GWs) is crucial for understanding the observed prevailing winds in the winter mesopause region and to explain observed GWs in the mesosphere and thermosphere.
- For small-enough spatial and temporal scales, observed GW spectra can be interpreted as stratified macro turbulence resulting from wave breaking.
- Higher-order GWs in the winter thermosphere explain observed day-time traveling ionospheric disturbances during periods of low geomagnetic activity.
- MSVC in the winter middle and upper atmosphere correlates with the strength of the polar vortex.
- The disturbances in the thermosphere and ionosphere that were caused by the Hunga Tonga-Hunga Ha'apai volcanic eruption were due to medium-to-large-scale secondary GWs.

# Multi-step vertical coupling via gravity waves from the lower to the upper atmosphere

Erich Becker<sup>a</sup>, Sharon L. Vadas<sup>a</sup>, Xinzhao Chu<sup>b</sup>

<sup>a</sup>*NorthWest Research Associates, Boulder Office, Boulder, CO, USA*

<sup>b</sup>*Cooperative Institute of Research in Environmental Sciences & Department of Aerospace Engineering Sciences, University of Colorado Boulder, Boulder, CO, USA*

---

## Abstract

We review the mechanism of multi-step vertical coupling (MSVC) via secondary and higher-order gravity waves (GWs), and its relevance for observed GW perturbations and the circulation in the upper mesosphere and thermosphere. Since the momentum deposition following the breaking or dissipation of a GW packet is localized in space and time, it leads to an imbalance in the ambient flow which in turn results in the generation of secondary or higher-order GWs. This local “body-force” (LBF) mechanism is essential for MSVC. We argue that small-scale secondary GWs resulting directly from GW instability form a macro-turbulent cascade that leads to the LBF. We present a simple scale analysis supporting this interpretation with respect to observed GW spectra. Several examples of MSVC are reviewed. These include 1) an explanation of the observed persistent GWs and prevailing eastward winds in the winter mesopause region at middle to high latitudes via secondary GWs, 2) evidence that many of the daytime traveling ionospheric disturbances in the F region during winter and low geomagnetic activity are driven by higher-order GWs from MSVC, 3) the dependence of MSVC during wintertime on the strength of the polar vortex, and 4) the secondary GW disturbances in the thermosphere and ionospheric that were triggered by the Tonga volcanic eruption on 15 January 2022. Furthermore, we describe the GW-resolving whole-atmosphere model that was primarily used in corresponding studies of MSVC, and we discuss some open questions.

**Keywords:** Multi-step vertical coupling (MSVC), secondary and higher-order gravity waves (GWs), local body-force mechanism, universal behavior of GW spectra, observations and modeling of MSVC

---

## Contents

<b>1</b>	<b>Introduction</b>	<b>2</b>
<b>2</b>	<b>Local body-force mechanism</b>	<b>5</b>
<b>3</b>	<b>Gravity-wave spectra and local body-force mechanism</b>	<b>7</b>
<b>4</b>	<b>Model description</b>	<b>11</b>
<b>5</b>	<b>Evidence of multi-step vertical coupling (MSVC)</b>	<b>13</b>
5.1	MSVC in the winter stratosphere and MLT . . . . .	13
5.2	MSVC in the winter thermosphere and ionosphere . . . . .	21
5.3	Secondary GWs from the Hunga Tonga-Hunga Ha’apai vol- canic eruption . . . . .	28
<b>6</b>	<b>Summary and some open questions</b>	<b>35</b>

## 1. Introduction

The global circulation in the upper mesosphere is mainly driven by the wave-mean flow interaction due to internal gravity waves (GWs) (Lindzen, 1981; Holton, 1983). Further contributions result from in-situ generated planetary waves (McLandress et al., 2006). The circulation is strongly driven by thermal tides in the lower thermosphere, and by ion drag at higher altitudes, while the average GW drag is minor in the mid and upper thermosphere (Becker, 2017; Becker et al., 2022a; Becker and Oberheide, 2023; Liu et al., 2024a). According to conventional wisdom (e.g., Smith, 2012; Becker, 2012), the GWs relevant for the circulation and variability in the stratosphere and mesosphere are of tropospheric origin. That is, they are primary GWs generated by flow over orography, deep moist convection, and spontaneous emission (fronts and jets) (see reviews of Fritts and Alexander, 2003; Plougonven and Zhang, 2014). In addition, primary GWs can be generated in the stratosphere by the polar vortex jet (e.g., Sato and Yoshiki, 2008; Sato et al., 2012; Becker et al., 2022b; Vadas et al., 2023a).

Recent studies suggest that the effects of GWs from “below” (i.e., from the troposphere and stratosphere) in the winter upper mesosphere and winter thermosphere during periods of low geomagnetic activity are due to secondary and higher-order GWs, not primary GWs (e.g., Becker and Vadas, 2018;

21 Vadas and Becker, 2019; Becker and Vadas, 2020; Xu et al., 2021; Becker  
 22 et al., 2022a; Vadas et al., 2024). According to theory (Vadas and Fritts,  
 23 2002; Vadas et al., 2003; Vadas, 2013; Vadas et al., 2018), secondary GWs  
 24 are excited from the imbalances that are created by the localized (in space  
 25 and time) wave-mean flow interactions (momentum and energy deposition)  
 26 that result from the breakdown of primary GW packets. Even though this  
 27 generation mechanism creates a broad spectrum of waves, the majority of the  
 28 secondary GWs have larger scales than the primary GWs. The secondary  
 29 GWs propagate upward and downward, and into all horizontal directions  
 30 away from the source region, except for the direction perpendicular to the  
 31 body force direction. They can account for significant non-local transport of  
 32 momentum and energy if their propagation directions and phase speeds in  
 33 relation to the background wind yield near-conservative upward propagation  
 34 for a few density scale heights. In such a case, amplitude growth due to  
 35 decreasing density with increasing height and wind shear (e.g., from tides)  
 36 will eventually cause the secondary GWs to break, or to dissipate directly  
 37 from molecular viscosity in the thermosphere, resulting in significant wave-  
 38 mean flow interaction. When this process is sufficiently localized in space and  
 39 time, tertiary GWs will be generated, and so forth. The vertical coupling  
 40 that results from primary to secondary and higher-order (tertiary, etc) GWs  
 41 has been dubbed “multi-step vertical coupling” (MSVC) (Vadas and Becker,  
 42 2019). The overall idea of this process is illustrated by the schematic in Fig.  
 43 1 for the winter hemisphere.

44 While GWs dissipate directly from kinematic molecular viscosity and heat  
 45 conduction at high altitudes in the thermosphere (Vadas, 2007), the dissipa-  
 46 tion scales are much smaller in the middle atmosphere where GWs undergo  
 47 complicated breaking processes when they reach a certain level of dynamic  
 48 instability. Theories have been brought forward to describe this process in  
 49 parametric form for application in global models (e.g. Lindzen, 1981; Hines,  
 50 1997; Medvedev and Klaassen, 2000; Becker and McLandress, 2009), and  
 51 high-resolution numerical simulations performed under idealized conditions  
 52 have provided an advanced understanding of the breaking processes that  
 53 occur under various circumstances regarding the background flow and inci-  
 54 dent GW characteristics (e.g. Achatz, 2007c,b,a; Dong et al., 2020). Most  
 55 importantly, the nonlinear interactions associated with GW breaking gener-  
 56 ate smaller-scale GWs which in turn generate even smaller-scale GWs due to  
 57 nonlinear interactions and so forth. In the statistical mean, this process must  
 58 be characterized by a forward energy cascade to higher wavenumbers (smaller



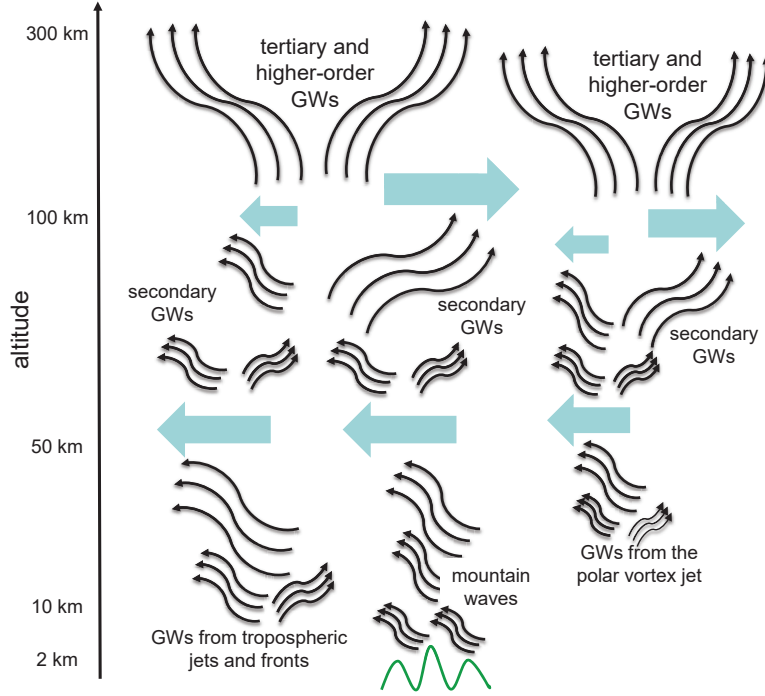


Figure 1: Schematic of multi-step vertical coupling (MSVC) in the winter hemisphere. Medium-scale primary GWs are generated by tropospheric jets and front, by flow over orography (indicated in green), and by the polar vortex jet. While mountain waves typically have westward intrinsic propagation directions, the other primary GWs can propagate into all horizontal directions. This is indicated by the black “wave-like” arrows below  $z \sim 50$  km. Mainly those primary GWs having westward propagation components propagate to the upper stratosphere and mesosphere where they dissipate from dynamic instability. The resulting westward drag components are indicated by the thick blue arrows. Due to the localized and intermittent character of this momentum deposition, secondary GWs are generated. With increasing height in the mesosphere, mainly those secondary GWs that have eastward propagation components reach the mesopause region. Here, these secondary GWs dissipate from the dynamic instability induced by the vertical wind shears associated with the semi-diurnal tide and traveling planetary waves, resulting in an eastward GW drag on average with regard to the zonal direction. This process leads to the generation of tertiary GWs, which propagate to higher altitudes in the thermosphere where they dissipate and may generate other higher-order GWs. Overall, the higher-order GWs in the thermosphere propagate into all horizontal direction. Those GWs propagating against the large-scale diurnal tidal winds in the winter thermosphere have the largest amplitudes at F region altitudes (above  $z \sim 250$  km). At these altitudes, the GWs dissipate directly from molecular viscosity and heat conduction. After Vadas and Becker (2019).

scales) that is initiated by the instability of the incident GW packet. These small-scale GWs must be distinguished from the secondary and higher-order GWs that give rise to MSVC. Even though some small-scale secondary GWs may also contribute to vertical coupling (Fritts et al., 2020), we will consider the small-scale GWs that contribute to the cascade to turbulence to be local. In other words, it is likely that most small-scale secondary and higher-order GWs do not transport momentum and energy far from the breaking region.

In this paper we review our current knowledge about MSVC and its role in wave phenomena and the circulation in the middle and upper atmosphere. In Sec. 2 we briefly review the aforementioned body-force mechanism. The importance of this mechanism for vertical coupling is further supported by showing that the observed universal behavior of observed GW spectra is likely a consequence of a macro-turbulent inertial range (Sec. 3). In Sec. 4 we give a brief description of the GW-resolving whole-atmosphere model that has mainly been used in published studies of MSVC. This is followed by a review of examples of MSVC in the literature (Sec. 5). We conclude with a summary and brief discussion of open questions in (Sec. 6).

## 2. Local body-force mechanism

The mechanism of a dissipating GW packet giving rise to secondary (or higher-order) GWs was first proposed by Vadas and Fritts (2002) and Vadas et al. (2003). In the latter paper, an idealized quasi-linear theory was presented in which the flow response to an imposed horizontal acceleration that was localized in space and time, dubbed local “body force” (LBF), was calculated using a Fourier-Laplace transform following Vadas and Fritts (2001). This analysis was revised in Vadas (2013) to include compressibility, and was applied in Vadas et al. (2018) where results from theory were compared to the first observational evidence of the LBF mechanism provided by lidar data from McMurdo Station (Antarctica). Figure 2 summarizes the major aspects of the flow response to a LBF. Several points should be noted:

- (1) The solution consists of an ambient (mean) flow response plus a broad spectrum of new (secondary) GWs. The ambient flow response is characterized by two counter-rotating cells (or vortices) in the horizontal plane. This response is simply the direct result of the acceleration by the body force and mass conservation, leading to return flows that are anti-parallel to the body force (see Fig. 2a).
- (2) The GWs excited by a LBF result from the imbalance that is generated

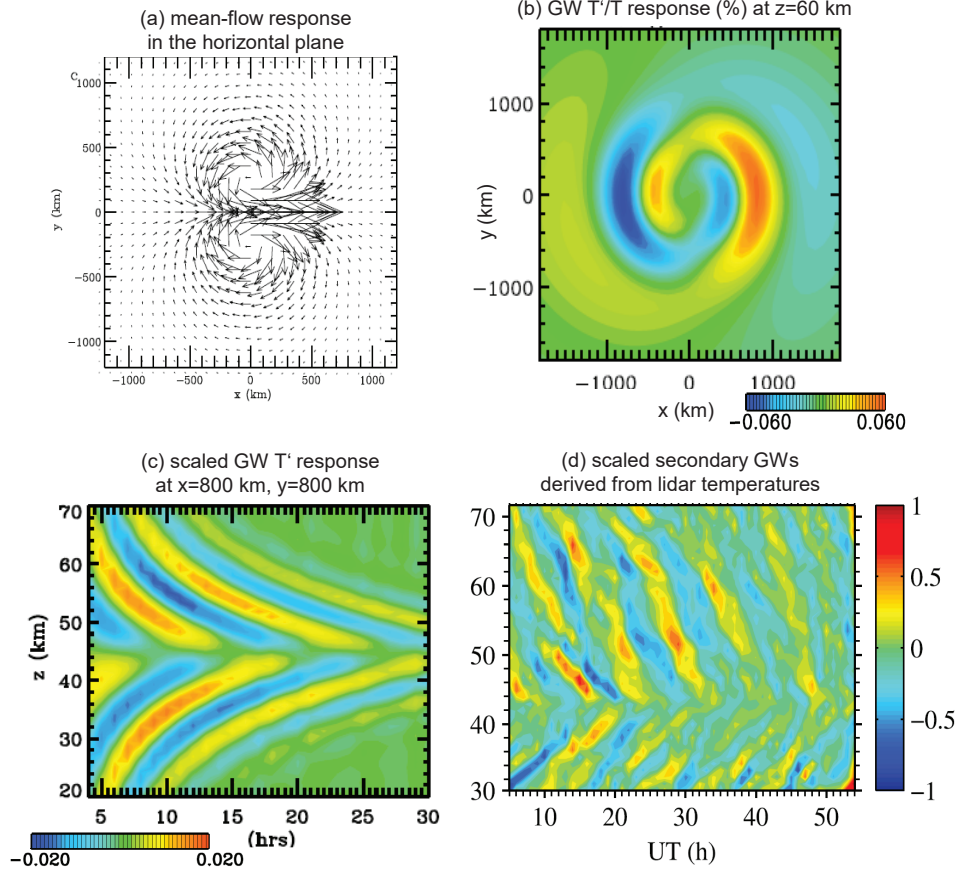


Figure 2: Illustration of the local body-force (LBF) mechanism. (a) Horizontal snapshot of the ambient horizontal-wind response predicted by theory at the height of a zonal LBF ( $z = 45$  km) and about 16 hr after the force is finished. The body force has full vertical, horizontal, and temporal widths of 8 km, 800 km, and 2 hours, respectively. Its maximum acceleration is  $120 \text{ m s}^{-1} \text{ d}^{-1}$ . (b) Corresponding GW relative temperature response at  $z = 60$  km and  $t = 4$  hr. (c) Corresponding time-height plot of the density-scaled relative GW temperature response,  $\sqrt{\rho} T'/T$ , in units of  $\sqrt{\text{g m}^3}$  as predicted by theory. (d) Density-scaled secondary GWs derived from lidar temperature observations at McMurdo Station ( $178^\circ \text{E}$ ,  $78^\circ \text{S}$ ), starting on 18 June 2014. The unit is  $10^{-3} \sqrt{\text{kg m}^3}$ . See Vadas et al. (2018, their Figs. 9, 13, and 15) for further details.

95 in the ambient flow. These secondary GWs consist of a broad spectrum of  
 96 waves. When the duration of the LBF is short enough, the largest GW am-  
 97 plitudes occur at horizontal and vertical wavelengths that are about twice  
 98 the length/width and height of the body force, respectively. The secondary  
 99 GWs propagate into all directions except perpendicular to the body force  
 100 (Fig. 2b).

101 (3) At a location that is horizontally displaced in a direction not perpendic-  
 102 ular of the body force, the GW response appears as a “fishbone structure”  
 103 in time-height plots of the temperature, density, and wind perturbations.  
 104 Figure 2c shows such a fishbone structure for the temperature response pre-  
 105 dicted by theory. The knee of this structure corresponds to the altitude of  
 106 the center of the body force.  
 107 (4) Rayleigh lidar temperature data from the stratosphere and lower meso-  
 108 sphere obtained in June 2014 at McMurdo Station (178°E, 78°S) was ana-  
 109 lyzed for fishbone structures. Figure 2d shows an example with the knee of  
 110 such a structure being located at  $z \sim 43$  km. The corresponding study by  
 111 Vadas et al. (2018) represents, to the best of our knowledge, the first obser-  
 112 vational confirmation of the LBF mechanism.  
 113 (5) For shorter duration and stronger spatial localization of a body force, the  
 114 secondary GWs have higher frequencies and larger wavenumbers. In the lim-  
 115 iting case of a body force that varies very slowly in time, no secondary GWs  
 116 are generated. This latter scenario corresponds to the implicit assumptions  
 117 made in conventional GW schemes (see discussions in Senf and Achatz, 2011;  
 118 Becker and Vadas, 2020; Bölöni et al., 2021).  
 119 (6) The theory of Vadas et al. (2003) and Vadas (2013) describes an idealized  
 120 picture of the secondary GW generation processes in the real atmosphere that  
 121 has certain limitations. For example, strong nonlinear interactions of GWs  
 122 can lead to body-force like perturbations of the ambient flow without the need  
 123 for a complete dissipation of a primary GW packet (e.g. Fritts et al., 2020;  
 124 Heale et al., 2022a). Furthermore, when there is a superposition of several  
 125 primary GW packets (which is most often the case), then the resulting LBFs  
 126 have smaller spatial and temporal scales than the LBF from a single primary  
 127 GW packet (Vadas and Crowley, 2010). Hence, the secondary GWs can have  
 128 smaller scales than the primary GWs. Finally, there is often a superposition  
 129 of secondary GWs from different LBFs; so it is not always straightforward  
 130 to identify the secondary GWs in measurements (Vadas et al., 2023a).

### 131 **3. Gravity-wave spectra and local body-force mechanism**

132 It is commonly believed that GWs having large horizontal wavenum-  
 133 bers and high frequencies are most important for vertical coupling. This  
 134 notion is rationalized by the following thought experiment. Consider two  
 135 mid-frequency GWs in the Boussinesq approximation that have the same  
 136 amplitudes (same energy densities). Then, the GW with the larger vertical

group velocity has the larger (absolute) vertical flux of horizontal momentum (hereafter: momentum flux) because 1) the momentum flux is equal to the energy density times  $k/m$ , where  $k$  and  $m$  are the absolute horizontal and vertical wavenumbers, respectively, and 2) the absolute intrinsic frequency is  $\omega_I = Nk/m$ , where  $N$  is the buoyancy frequency. This “equal amplitude” argument suggests that for a given vertical wavelength, GWs having smaller horizontal scales (larger  $k$ ) or, generally, GWs having larger  $\omega_I$  should account for larger momentum flux. In the following we show that the observed GW energy spectra suggest that on average, both the GW amplitudes and the GW momentum fluxes are smaller for increasing horizontal wavenumber or for increasing frequency (decreasing horizontal wavelength or decreasing period), thereby negating the relevance of the “equal-amplitude” though experiment.

Observed vertical wavenumber spectra of GWs often show a universal behavior with a  $m^{-3}$  exponential slope. This observation can be explained by assuming that all the GWs contributing to the spectrum are at the saturation level (Smith et al., 1987; Fritts and Alexander, 2003). Alternatively, Lindborg (2006) speculated that this universal behavior of observed vertical wavenumber spectra is a reflection of a macro-turbulent inertial range governed by the scaling laws of stratified (macro-)turbulence (hereafter: SMT). Such a cascade would be induced by GW packets that have become dynamically unstable, leading to GW breaking and a cascade to smaller and smaller GWs, which would then also have smaller and smaller periods, until the macro-turbulent cascade transits into Kolmogorov turbulence at the Ozmidov scale (e.g., Avsarkisov et al., 2022). This hypothesis was recently supported by Knobloch et al. (2023) who found the  $k^{-5/3}$  spectral behavior in the observed GW horizontal wavenumber spectra. Precisely such a horizontal wavenumber spectrum is predicted by SMT. Our following scaling analysis shows that for SMT, 1) the finding of Smith et al. (1987) is quantitatively consistent with SMT, 2) GW frequency power spectra should have a functional behavior between  $\omega^{-5/3}$  and  $\omega^{-2}$  ( $\omega$  = ground-based frequency), and 3) the vertical flux of horizontal momentum decreases with increasing horizontal wavenumber and increasing frequency.

SMT assumes a forward energy cascade with regard to the horizontal scales. Hence, the usual scaling analysis from classical turbulence predicts

$$e_k \sim \frac{2}{3} \epsilon^{2/3} k^{-5/3} \quad (1)$$

172 for the power spectrum of the horizontal wind,  $e_k$ . Here,  $\epsilon$  is the mechanical  
 173 dissipation (or frictional heating) rate per unit mass. The scale-dependent  
 174 aspect ratio for SMT can be written as (Lindborg, 2006; Brune and Becker,  
 175 2013)

$$k = \frac{\epsilon}{N^3} m^3 \quad \leftrightarrow \quad m = N \epsilon^{-1/3} k^{1/3}. \quad (2)$$

176 Plugging the first equation (2) into (1) and using  $e_m = e_k(dk/dm)$ , the  
 177 vertical wavenumber spectrum is

$$e_m \sim 2 N^2 m^{-3}, \quad (3)$$

178 which is often observed at various locations and for ranges of scales (e.g.,  
 179 Chu et al., 2018). Alternatively, to obtain the traditional interpretation of  
 180 the  $m^{-3}$ -spectrum for GWs as proposed by Smith et al. (1987), we assume a  
 181 spectrum of saturated GWs subject to the mid-frequency and Boussinesq ap-  
 182 proximations. The saturation condition is  $m|T'| = g/c_p$  for the temperature  
 183 perturbation amplitude  $T'$  (Lindzen, 1981). We now use the polarization  
 184 relations  $\omega_I|T'| = (g/c_p)|w'|$  and  $k|u'| = m|w'|$ , where  $u'$  and  $w'$  are the GW  
 185 horizontal and vertical wind perturbations, respectively, as well the GW dis-  
 186 persion relation  $\omega_I = Nk/m$ . Then the saturation condition can be written  
 187 as  $|u'| \sim N/m$ . Furthermore, the integral-scale GW horizontal wind ampli-  
 188 tude  $u_a$  at wavenumber  $m$  is defined as

$$u_a^2 \sim \int_m^\infty e_{m'} dm'. \quad (4)$$

189 Assuming that  $u_a$  fulfills the saturation condition, we get

$$N^2 m^{-2} \sim \int_m^\infty e_{m'} dm' \quad \rightarrow \quad e_m \sim 2 N^2 m^{-3}, \quad (5)$$

190 which is equivalent to Eq. (3). Hence, if an SMT inertial range is governed  
 191 by the nonlinear interactions of GW modes that fulfill the mid-frequency  
 192 and Boussinesq approximations, then these GW modes assume integral-scale  
 193 amplitudes that correspond to the saturation condition.

194 To obtain the GW frequency spectra in the case of SMT, we assume first  
 195 that the background wind is zero, which allows us to estimate the intrinsic  
 196 frequency spectrum. Combining the first Eq. (2) with the dispersion relation,  
 197  $\omega_I = Nk/m$ , yields

$$\omega_I = \epsilon N^{-2} m^2 \quad \leftrightarrow \quad m = N \omega_I^{1/2} \epsilon^{-1/2}. \quad (6)$$

198 This expression can be used to transform the vertical wavenumber spectrum  
 199 (3) into an intrinsic wavenumber spectrum as follows:

$$e_{\omega_I} = e_m(dm/d\omega_I) \sim \epsilon \omega_I^{-2}. \quad (7)$$

200 Since ground-based measurements usually observe GWs subject to Doppler  
 201 shifting by the background wind such that  $\omega_I \geq \omega$  for GWs propagating  
 202 against the background wind, Eq. (7) is considered to be a lower limit for  
 203 the observed frequency spectra. The corresponding upper limit is obtained  
 204 by noting that  $\omega_I^3 = (\omega - kU)^3$ , where  $U$  denotes the (absolute) background  
 205 wind. Using Eqs. (6) and (2), we get  $(\omega - kU)^3 = \epsilon k^2$ . Solving for the  
 206 ground-based frequency yields

$$\omega = kU + \epsilon^{1/3} k^{2/3} \quad (8)$$

207 For large-enough  $k$ , the first term on the right-hand side of Eq. (8) will  
 208 become larger than the second term, hence

$$\omega = kU \quad \text{for finite } U \text{ and large } k. \quad (9)$$

209 Using Eq. (9), the horizontal wavenumber spectrum (1) can be converted  
 210 into

$$e_\omega = e_k(dk/d\omega) \sim \frac{2}{3} \epsilon^{2/3} U^{2/3} \omega^{-5/3}. \quad (10)$$

211 Observed frequency spectra of GWs usually have exponential slopes between  
 212  $-5/3$  and  $-2$  (e.g., Hoffmann et al., 2010; Guo et al., 2017; Podglajen et al.,  
 213 2016; Sato et al., 2016; Chen et al., 2016). Equations (7) and (10) prove  
 214 that these observations are, like the aforementioned result of Knobloch et al.  
 215 (2023) for GW horizontal wavenumber spectra and the well-known vertical  
 216 wavenumber spectra, compatible with the hypothesis of a macro-turbulent  
 217 inertial range. That is, the assumption of SMT combined with the GW  
 218 dispersion and polarizations relations predicts all these spectra. The as-  
 219 sumption of GW saturation, on the other hand, can predict only the vertical  
 220 wavenumber spectrum.

221 We now estimate the GW momentum flux spectra that are expected  
 222 for SMT. Assuming again the mid-frequency and Boussinesq approximation  
 223 for the GWs, the momentum flux spectra with regard to either  $k$  or  $m$  are  
 224 obtained by multiplying the energy spectra (1) or (3) with  $k/m$ , where either

225  $m$  or  $k$  is eliminated according to the scale-dependent aspect ratio of SMT  
 226 (Eq. (2)). The resulting momentum flux spectra are

$$f_k = e_k k/m \sim \frac{2}{3} \epsilon N^{-1} k^{-1} \quad \text{and} \quad f_m = e_m k/m \sim 2 \epsilon N^{-1} m^{-1}. \quad (11)$$

227 These estimates show that the momentum flux decreases for smaller hori-  
 228 zontal scales when the scaling laws of SMT apply. Using Eqs. (6) or (9), the  
 229 momentum flux spectra (11) can be converted into frequency space:

$$f_{\omega_I} = f_m (dm/d\omega_I) \sim \epsilon N^{-1} \omega_I^{-1} \quad \text{and} \quad f_{\omega} = f_k (dk/d\omega) \sim \frac{2}{3} \epsilon N^{-1} \omega^{-1}. \quad (12)$$

230 Hence, the spectral momentum flux decreases with increasing frequency in  
 231 the case of SMT. Such a behavior has been found in radar observations in  
 232 the upper mesosphere at high latitudes for periods shorter than a few hours  
 233 by Sato et al. (2017).

234 Summarizing, the observed universal behavior of GW spectra for small-  
 235 enough scales and periods suggests a macro-turbulent inertial range governed  
 236 by SMT. In particular, the spectral momentum flux decreases with increasing  
 237 wavenumber and increasing frequency. This analysis supports the relevance  
 238 of the local body-force (LBF) mechanism described in Sec. 2 since small-scale  
 239 secondary GWs resulting from the breaking of medium-scale GWs will not  
 240 contribute efficiently to vertical coupling. Rather, due to the forward cascade  
 241 associated with the inertial range, these wave modes eventually result in the  
 242 LBF. The imbalance of the ambient flow then gives rise to vertically prop-  
 243 agating secondary GWs that contribute to vertical coupling. Furthermore,  
 244 medium-scale primary GWs may contribute substantially to the momentum  
 245 and energy transfer from the troposphere to the middle atmosphere. These  
 246 GWs are resolved successfully in current high-resolution whole-atmosphere  
 247 models (e.g., Becker et al., 2022b,a; Vadas et al., 2023a; Liu et al., 2024b).

#### 248 4. Model description

249 The Kühlungsborn Mechanistic general Circulation Model (KMCM) was  
 250 the first GW-resolving general circulation model (GCM) showing that sec-  
 251 ondary GWs are substantial for understanding the general circulation in the  
 252 winter mesosphere and lower thermosphere (MLT) (Becker and Vadas, 2018).  
 253 The HIgh Altitude Mechanistic general Circulation Model (HIAMCM) is a



vertical extension of the KMCM with a variety of new components and further developments.

The HIAMCM simulates the neutral dynamics from the surface to the upper thermosphere. It is based on a spectral dynamical core with a terrain-following hybrid vertical coordinate (Simmons and Burridge, 1981). It is currently run with a spectral resolution of T256 (truncation at a total horizontal wavenumber of 256), which corresponds to a horizontal grid-spacing of  $\sim 52$  km and a shortest resolved horizontal wavelength of  $\lambda_h \sim 156$  km. The effective horizontal resolution is  $\lambda_h \sim 200$  km (Becker et al., 2022b). The vertical level spacing is  $\sim 600 - 650$  m between the boundary layer and  $3 \times 10^{-5}$  hPa ( $z \sim 130$  km), and increases with altitude above that level, reaching  $\sim 10$  km above  $z \sim 300$  km. Using 280 full layers (L280), the model top is at  $4 \times 10^{-9}$  hPa, corresponding to  $z \sim 450$  km for temperatures of  $T \sim 950$  K above  $\sim 250$  km. The dynamical core is equipped with a correction for non-hydrostatic dynamics and a thermodynamically consistent extension into the thermosphere (Becker and Vadas, 2020).

The HIAMCM includes explicit computations of radiative transfer and water vapor transport, parameterizations of large-scale condensation and moist convection, as well as the full surface energy budget combined with a slab ocean and full topography. Macro-turbulent vertical and horizontal diffusion is parameterized by the classical Smagorinsky model, with the diffusion coefficients depending on the local Richardson number,  $Ri$ , giving rise to strong wave damping for  $Ri \leq 0.25$  (Becker and Burkhardt, 2007; Becker, 2009). The diffusion scheme accommodates molecular viscosity in the thermosphere for both vertical and horizontal diffusion. As a result, molecular viscosity is the predominant dissipation mechanism for resolved GWs above  $z \sim 200$  km (Vadas, 2007; Becker and Vadas, 2020). A simple ion-drag scheme is applied to account for the neutral-ion coupling at low and middle altitudes. The parameterized ion drag furthermore includes a forcing of the auroral circulation in the polar thermosphere (Forbes, 2007; Becker et al., 2022a).

To allow for direct comparison with observational data, the HIAMCM can be nudged to MERRA-2 reanalysis in the troposphere and stratosphere. This nudging is performed in spectral space and is restricted to the planetary-and-synoptic-scale flow. As a result, the explicit simulation of GWs is preserved since GWs are not directly affected by the nudging (Becker et al., 2022b).

The radiation and moist convection schemes are simplified compared to methods used in community models. Furthermore, the HIAMCM does not include a chemistry module, and ion drag is the only ionospheric process that

is accounted for. To distinguish these idealizations from methods employed in comprehensive community models, the HIAMCM is called a “mechanistic” model.

## 5. Evidence of multi-step vertical coupling (MSVC)

### 5.1. MSVC in the winter stratosphere and MLT

Even though the body-force mechanism for GW generation was proposed in the early 2000s, it took about ten years until the first applications of this mechanism under realistic conditions were published (Vadas and Liu, 2009, 2013; Vadas et al., 2014). These modeling studies focused on secondary GWs in the thermosphere that were generated from the dissipation of convectively generated primary GWs. Later on, the possible fundamental role of MSVC in the winter mesosphere and lower thermosphere (MLT) was suggested by lidar observations of GWs at McMurdo Station in Antarctica (Chu et al., 2011; Chen et al., 2013). These observations showed persistent large-amplitude GWs having medium-to-inertial frequencies and large vertical wavelengths in the winter mesopause region (Chen et al., 2016). In addition, horizontal wavelengths of  $\lambda_h \sim 300 - 500$  km in the stratosphere that were inferred by Zhao et al. (2017) were found to be much shorter than the  $\lambda_h \sim 800 - 3000$  km estimates by Chen and Chu (2017) for the mesopause region. Such a significant change in  $\lambda_h$  with altitude suggested that the GWs in the mesopause region were secondary, not primary, GWs.

Becker and Vadas (2018) used the free-running KMCM with resolved GWs to simulate the general circulation. They chose several days during June and compared the simulated GWs with lidar observations at McMurdo Station in Antarctica (Chen et al., 2016). Figure 3a shows the observed relative temperature perturbations that were obtained by spectral filtering to retain only periods shorter than 12 hours. The corresponding model result is shown in Fig. 3b. Strong GW amplitudes are seen in the MLT in both plots. These results are unexpected during the wintertime when assuming that primary GWs are the predominant GWs in the middle atmosphere. In particular, only very weak primary GW activity is expected in the winter mesopause region (e.g., Lindzen, 1981; Becker, 2012; Becker and Vadas, 2018). Moreover, the vertical wavelengths of the GWs in Fig. 3 are much longer in the mesopause region than in the stratosphere. This is surprising since during the wintertime, primary GWs propagate predominantly westward in the upper stratosphere and lower mesosphere due to dynamic in-

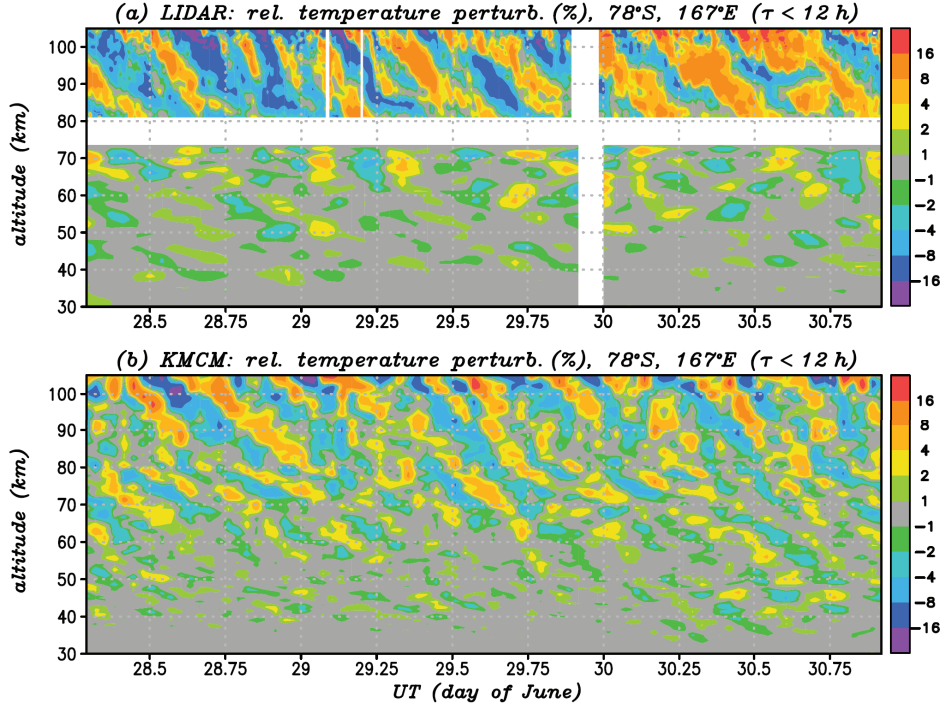


Figure 3: Temperature perturbations at McMurdo (Antarctica) during late June. The perturbations include only periods shorter than 12 hr. (a) From ground-based lidar measurements of Chen et al. (2016). (b) From the KMCM simulation. See Becker and Vadas (2018) for further details.

328 stability of eastward propagating primary GWs at lower altitudes (Lindzen,  
 329 1981; Holton, 1983). Therefore, the vertical wavelengths of the primary GWs  
 330 would decrease with altitude in the upper mesosphere (rather than increase)  
 331 since here the strength of the eastward flow associated with the polar vortex  
 332 decreases with altitude. Hence, the observed and simulated GWs in  
 333 the mesopause region as shown in Fig. 3 are very likely eastward propagat-  
 334 ing. Additionally, the simulated horizontal wavelengths in the stratosphere  
 335 and upper mesosphere were consistent with the aforementioned estimates  
 336 of Zhao et al. (2017) and Chen and Chu (2017), respectively (Vadas and  
 337 Becker, 2018). These considerations demonstrate that the GWs observed in  
 338 the mesopause region are not the same GWs as those that govern the GW  
 339 field in the stratosphere and lower mesosphere. Rather, most of the GWs  
 340 at  $z > 70$  km during the wintertime at McMurdo Station are most likely  
 341 secondary GWs.

342 Further analysis of the model and lidar data showed that the GWs in

343 the southern winter mesopause region were indeed generated in the upper  
 344 stratosphere and lower mesosphere by the body-force mechanism (Becker  
 345 and Vadas, 2018; Vadas and Becker, 2018; Vadas et al., 2018). These studies  
 346 furthermore revealed that the wintertime secondary GWs play a fundamental  
 347 role for the general circulation. This is illustrated in Fig. 4. The upper row  
 348 in the figure shows the simulated zonal-mean zonal wind in the southern  
 349 winter hemisphere from the GW-resolving KMCM and from a corresponding  
 350 course-resolution model version where orographic and non-orographic GWs  
 351 were parameterized based on the methods of McFarlane (1987) and Becker  
 352 and McLandress (2009), respectively (conventional model setup). The overall  
 353 structure of the zonal wind is quite reasonable and comparable for the two  
 354 model versions in the stratosphere and lower mesosphere. The GW-resolving  
 355 simulation exhibits prevailing eastward winds at middle to high latitudes  
 356 also in the upper mesosphere and lower thermosphere. The conventional  
 357 model setup, however, produces a wind reversal to westward flow in the  
 358 upper mesosphere. Such a wind reversal is a general but unrealistic feature  
 359 of models with parameterized GWs (Smith, 2012). Recently, this deficit  
 360 of conventional models was further analyzed by Hindley et al. (2022) and  
 361 Harvey et al. (2022).

362 The colors in the lower panels in Fig. 4 show the vertical fluxes of zonal  
 363 momentum per unit mass due to resolved GWs (panel c) and parameterized  
 364 GWs (panel d). As expected, the westward momentum flux in the conven-  
 365 tional model setup is maximum in the stratopause region and decreases to  
 366 zero with increasing height. When GWs are simulated explicitly, this pat-  
 367 tern of the westward momentum flux is reproduced (albeit with somewhat  
 368 smaller values), but is complemented by a significant eastward momentum  
 369 flux at higher altitudes. This eastward flux leads to a significant eastward  
 370 GW drag in the winter polar mesopause region in addition to the usual west-  
 371 ward GW drag from primary GWs in the stratosphere and lower mesosphere  
 372 (contours in Fig. 4c and d). Even though thermal tides and traveling plan-  
 373 etary waves also contribute to the wave driving in the mesopause region, it  
 374 is the eastward GW drag from the secondary GWs that leads to a realistic  
 375 zonal wind in this regime. Therefore, MSVC is not only important for the  
 376 interpretation of observed GW perturbations (Fig. 3), but is also an essential  
 377 new element in our understanding of the general circulation in the MLT.

378 It may be argued that the eastward GW drag in the winter mesopause re-  
 379 gion is due to primary GWs having large horizontal phase speeds that were  
 380 not included in the non-orographic GW scheme of the KMCM (or corre-

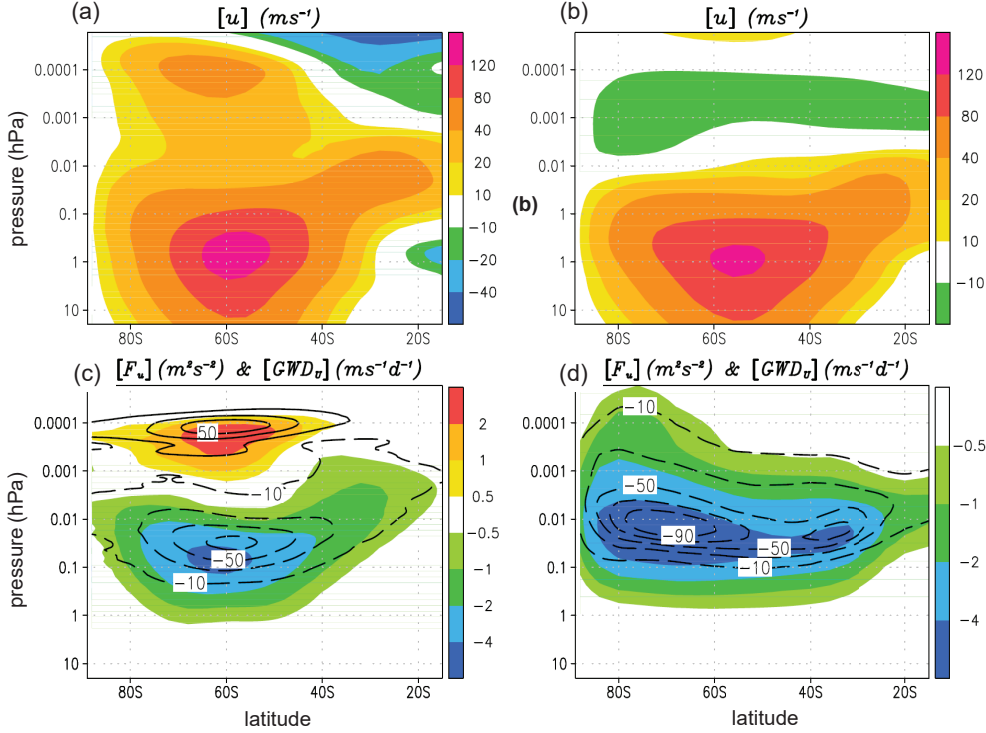


Figure 4: Resolved versus parameterized GWs. Comparison of the high-resolution KMCM with resolved GWs (left column) and a corresponding course-resolution model version with parameterized GWs (right column) in the southern winter hemisphere (averaged from June 21 to August 10). Upper row: Zonal-mean zonal wind. Lower row: Vertical flux of zonal momentum due to GWs (color shading) and GW drag (contours for 0,  $\pm 30$ ,  $\pm 50$ ,  $-70$ ,  $-90$   $\text{m s}^{-1} \text{d}^{-1}$ ). For the GW-resolving HIAMCM, GW perturbations are defined by retaining only total horizontal wavenumbers  $n > 30$  (horizontal wavelengths  $\lambda_h < 1350$  km) with respect to the spectral decomposition in terms of the spherical harmonics. The pressure levels correspond to the model’s vertical hybrid coordinate times 1013 hPa. See Becker and Vadas (2018) for further details.

381 sponding GW schemes in other models). However, the southern polar vortex  
 382 is characterized by large mean winds so that these primary GWs would need  
 383 to have extremely large eastward phase speeds to avoid critical levels. More  
 384 importantly, if primary GWs accounted for the eastward GW drag in Fig.  
 385 4c, then this effect should be even larger during wintertime in the northern  
 386 hemisphere since here the polar vortex is much weaker than in the southern  
 387 winter hemisphere so that more primary GWs having eastward phase speeds  
 388 and eastward momentum flux would reach the MLT. However, the opposite  
 389 was simulated with the GW-resolving KMCM. The eastward zonal flow and  
 390 resolved GW activity in the winter mesopause region are stronger during

July than during January (Becker et al., 2020; Avsarkisov et al., 2022). This hemispheric asymmetry is consistent with satellite observations that also show stronger eastward winds in the winter polar mesopause region during July than during January (Smith, 2012).

Figure 5 shows the zonal-mean circulation for the whole atmosphere from the HIAMCM for 1–20 January 2017 (left column) and 6–20 July 2006 (right column). The HIAMCM simulates reasonably realistic temperatures and zonal winds. This includes the cold summer mesopause and the transition from westward to eastward flow above the temperature minimum, the subtropical mesospheric jet in the winter hemisphere, as well as eastward winds at high latitudes in the winter MLT. The hemispheric differences when comparing July to January include a stronger eastward flow and stronger westward Eliassen-Palm flux (EPF) divergence in the winter stratosphere and lower mesosphere, stronger absolute EPF divergence in the upper mesosphere and a stronger summer-to-winter pole residual circulation and a colder summer polar mesopause. These hemispheric differences are consistent with satellite observations and the interhemispheric coupling mechanism (e.g. Karlsson and Becker, 2016; K rnich and Becker, 2010; Smith, 2012). The eastward flow and eastward EPF divergence in the winter mesopause region is stronger during July than January. According to our discussion above, this hemispheric difference is caused by stronger secondary GW generation when the polar vortex is stronger. For these particular model simulations, also the westward EPF divergence in the summer lower thermosphere is stronger during July. As a result of these hemispheric differences, the reversed residual circulation cell in the lower thermosphere is stronger during July and extends from pole to pole.

The dependence of secondary GWs in the winter upper mesosphere on the polar vortex strength farther below was explained in Vadas and Becker (2019) and Vadas et al. (2024) based on the LBF mechanism. Consider a primary GW packet generated at a height around  $z_i$ , propagating upward nearly conservatively, and then dissipating around  $z_b > z_i$ , thereby creating a LBF at  $z_b$  that induces the generation of secondary GWs. The secondary GW amplitudes are proportional to the body force. Considering those secondary GWs at a height  $z > z_b$  that propagate nearly conservatively, their amplitudes can be estimated to be proportional to  $\exp\{(z_b - z_i)/H\} \times \exp\{(z - z_b)/(2H)\} = \exp\{(z + z_b - 2z_i)/(2H)\}$ , where  $H$  is the density scale height. This equation means that under idealized conditions, the secondary GW generation according to the LBF mechanism works like an amplifier for the GWs at  $z > z_b$ ,

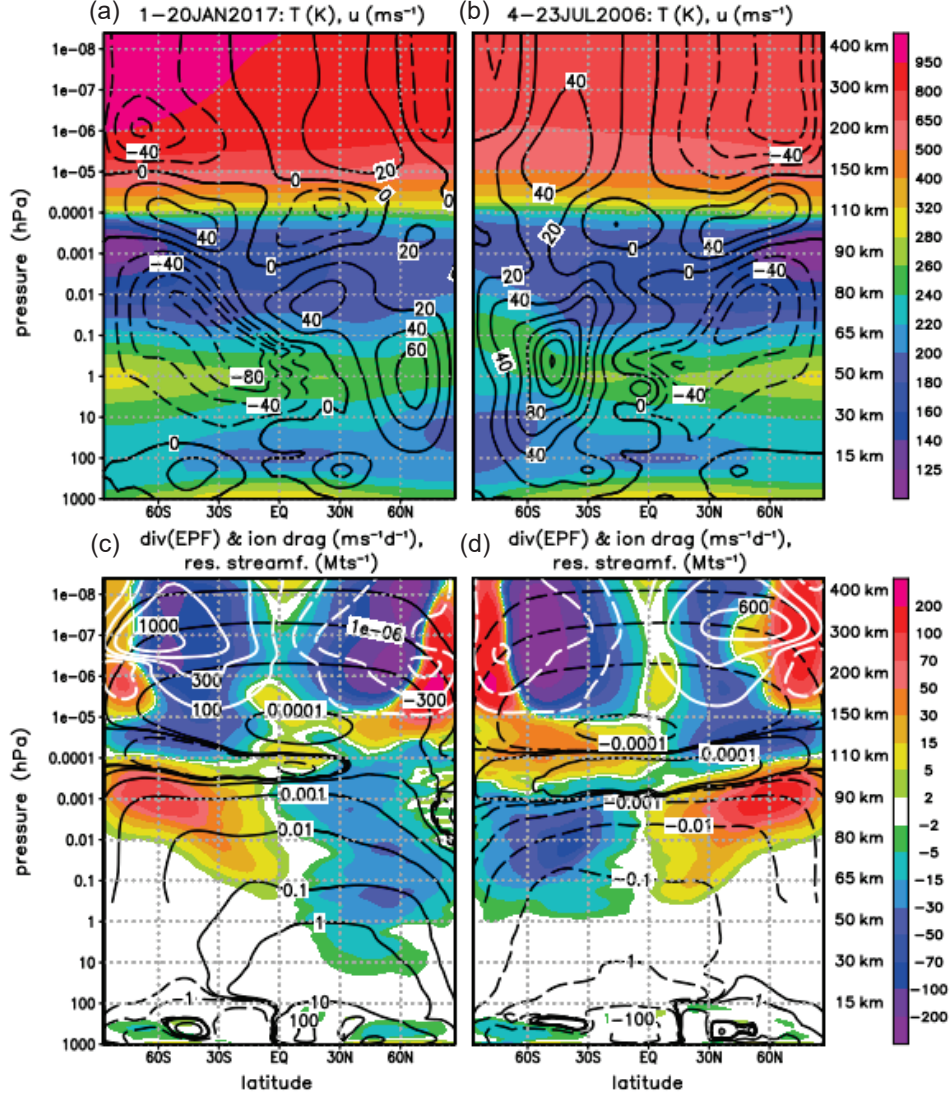


Figure 5: Zonal-mean circulation and wave driving from the HIAMCM for 1-20 January 2017 (left) and 6-20 July 2006 (right). First row: Temperature (colors) and zonal wind (contour interval 20 m/s). Second row: Eliassen-Palm flux (EPF) divergence (colors, unit  $\text{ms}^{-1}\text{d}^{-1}$ ), residual mass streamfunction (black contours) and zonal component of the parameterized ion drag (white contours). Black contours in (c) are for  $10^{-7}, 10^{-6}, \pm 10^{-5}, \pm 10^{-4}, 10^{-3}, 10^{-2} \text{ Mts}^{-1}$  above 0.3 hPa and for  $\pm 0.1, \pm 1, \pm 10, 100 \text{ Mts}^{-1}$  in the troposphere and stratosphere. Black contours in (d) are as in (c), but with opposite sign. White contours in (c) and (d) are for  $\pm 100, \pm 300, \pm 600, 10^3 \text{ ms}^{-1}\text{d}^{-1}$ . The pressure levels correspond to the model's vertical hybrid coordinate times 1013 hPa. Approximate heights are given on the right-hand sides of panel b and d.

429 resulting in larger amplitudes when  $z_b$  shifts to higher altitudes. Since pri-  
 430 mary westward GWs break at higher altitudes for a stronger polar vortex,  
 431 the secondary GWs in winter mesopause region along with their eastward  
 432 GW drag are also stronger in this case. This simple estimate explains why  
 433 the EPF flux divergence from about  $1 \times 10^{-3}$  to  $3 \times 10^{-5}$  hPa (about 90 to  
 434 120 km) as simulated by the HIAMCM is more eastward in the southern  
 435 winter hemisphere (Fig. 5d, left half of the panel) than in the northern win-  
 436 ter hemisphere (Fig. 5c, right half of the panel). It also explains why the  
 437 model fidelity in the northern winter MLT of conventional whole-atmosphere  
 438 models with parameterized GWs (hence, no MSVC) is enhanced during pe-  
 439 riods of a weak and variable polar vortex (including sudden stratospheric  
 440 warming events), but is very low when the polar vortex is strong and stable  
 441 (Harvey et al., 2022). The reason is that secondary (and higher-order) GWs  
 442 are highly relevant in the latter case and much less so in the former case.

443 The primary GWs that give rise to MSVC in the winter hemisphere are  
 444 not necessarily due to only tropospheric sources (e.g., flow over topography  
 445 and jets and fronts). Recent studies suggest that GWs generated by the  
 446 polar vortex jet give rise to significant contributions as well (Vadas et al.,  
 447 2023a, 2024). Figure 6 compares GWs simulated by the HIAMCM with lidar  
 448 observations at the ALOMAR observatory in northern Norway in January  
 449 2016. In this case study, several fishbone structures were observed by the lidar  
 450 and simulated by the HIAMCM at about the same heights and with about  
 451 the same timing and amplitudes. As discussed in Sec. 2, such structures  
 452 are indicative of GW generation from several LBFs at horizontally displaced  
 453 locations. Analysis of the HIAMCM data showed that the location of the  
 454 first LBF was about 1500 km farther southeast, and that the primary GWs  
 455 giving rise to the LBF were generated from the polar vortex jet in the lower  
 456 stratosphere (Vadas et al., 2023a).

457 High-resolution direct measurements of the vertical wind, temperature,  
 458 and metal species in the Antarctic mesopause region in late May 2020 with  
 459 a Na Doppler lidar profiled the vertical fluxes of sensible heat and meteoric  
 460 species (Chu et al., 2022). This study found that a significant portion of the  
 461 observed wintertime GWs propagated downward between  $\sim 89$  and 95 km.  
 462 Furthermore, the GW potential energy per unit mass exhibited two local  
 463 maxima around 85 and 112 km. According to the model study of Vadas  
 464 and Becker (2019, their Fig. 20), the first and second maximum in the lidar  
 465 data likely reflected the dissipation of mainly primary and secondary GWs,  
 466 respectively. Hence, the observed downward propagating GWs between the



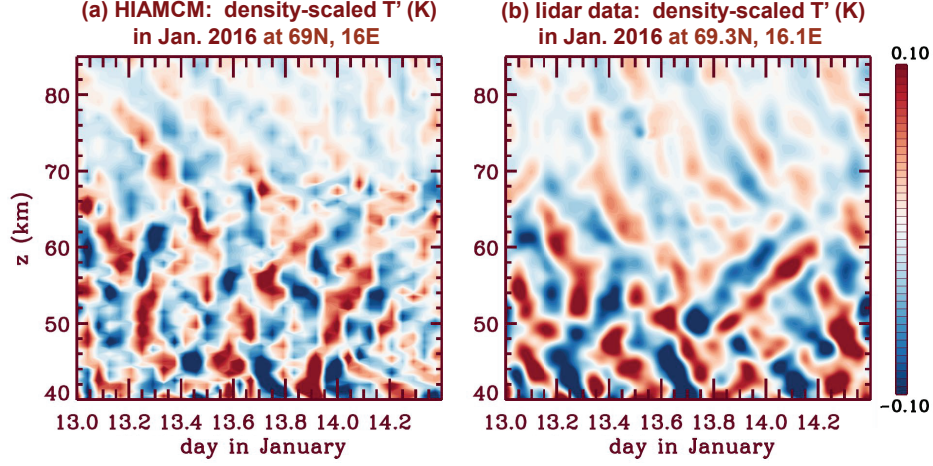


Figure 6: (a) Scaled temperature perturbations  $T' \times \exp(-z/2H)$  ( $H=7$  km) on 12-14 January 2016 from the HIAMCM at the site of the ALOMAR observatory in northern Norway. (b) Corresponding result from lidar observations. See Vadas et al. (2023a) for further details.

two energy maxima were likely tertiary GWs generated by the dissipation of secondary GWs at  $\sim 112$  km. These observations lend further support to the importance of MSVC to explain GW observations in the winter MLT.

Large-amplitude GWs during wintertime in the northern hemisphere at altitudes above  $z \sim 85$  km were found in radar observations by Hoffmann et al. (2010, their Fig. 11), but were not identified as secondary GWs at that time. Furthermore, Avsarkisov et al. (2022) computed the annual cycle of the integral turbulent velocity based on radar measurements in the northern hemisphere (see Fig. 10 in their paper). This result reflected the well-known summer-winter asymmetry that is expected for the primary GW amplitudes (e.g., Lindzen, 1981; Becker, 2012), namely a large maximum in the summer mesopause region and a weaker maximum in the winter lower mesosphere. This summer-winter asymmetry is consistent with former rocket-borne measurements of the turbulent dissipation rate by Lübken (1997, see his Figs. 7 and 8). In addition, the result of Avsarkisov et al. (2022) showed a pronounced secondary maximum of the integral turbulent velocity above  $z \sim 90$  km during wintertime. This secondary maximum is likely due to secondary GWs. Hence, the results of Hoffmann et al. (2010) and Avsarkisov et al. (2022) confirm that secondary GWs are relevant also in the northern winter hemisphere. It is likely that the rocket-borne measurements of Lübken

487 (1997) did not reach high enough to capture the dissipation induced by the  
488 breaking of the wintertime secondary GWs.

## 489 5.2. MSVC in the winter thermosphere and ionosphere

490 The dependence of MSVC in the winter middle atmosphere on the polar  
491 vortex translates into the winter thermosphere and ionosphere. This state-  
492 ment holds particularly true for low geomagnetic activity. A link between  
493 the polar vortex and GWs in the thermosphere during geomagnetically quiet  
494 times was found by Frisell et al. (2016) and Nayak and Yigit (2019). These  
495 observational studies showed that wintertime traveling ionospheric distur-  
496 bances (TIDs) at middle latitudes during daytime in the northern hemisphere  
497 are correlated with the strength of the polar vortex. Since most quiet-time  
498 TIDs are likely caused by GWs from below, this correlation suggests that  
499 the strengths of wintertime thermospheric GWs and the polar vortex are  
500 positively correlated as well. We therefore expect a pronounced effect when  
501 comparing particular periods with a strong polar vortex to periods character-  
502 ized by a weak polar vortex or even a sudden stratospheric warming (SSW)  
503 event. Becker et al. (2022a) addressed the corresponding dynamical mech-  
504 anism by analyzing a HIAMCM simulation for the winter 2016-2017. This  
505 season was characterized by a strong vortex in late December 2016 and an  
506 SSW event in late January and early February 2017. In the following we  
507 review some results of this study.

508 Figure 7a,b shows snapshots of GW temperature perturbations and large-  
509 scale winds at 60°N and 12 UT on 27 December 2016 (strong vortex period).  
510 We use the same wavenumber decomposition based on spherical harmonics  
511 to distinguish between the large-scale flow and GWs as in Fig. 4. Panel a  
512 indicates strong primary GWs in the stratosphere and lower mesosphere over  
513 northern Europe (from about 10°W to 20°E). The phase inclination of these  
514 GWs is indicative of westward propagation relative to the mean flow. The  
515 flattening of the GW phases in the lower mesosphere over Europe indicates  
516 dynamical instability and subsequent dissipation induced by turbulent diffu-  
517 sion, leading to GW-mean flow interaction. This process is induced by the  
518 Doppler shifting of the westward GWs towards smaller intrinsic frequencies  
519 (shorter vertical wavelengths) caused by westward vertical wind shear (see  
520 color in panel b). Similar GW features as over Europe are seen in other lon-  
521 gitude bands, for example, from about 90°E to 110°E and from about 140°E  
522 to 160°E. In view of the MSVC mechanism discussed above, Fig. 7a suggests  
523 that secondary GWs become the predominant GWs in the winter mesosphere

524 for  $z \sim 70 - 100$  km. The phase inclinations of these GWs are indicative of  
 525 both westward and eastward propagation directions, with eastward propaga-  
 526 tion prevailing with increasing altitude because of westward vertical shear of  
 527 the large-scale zonal wind (colors in panel b). For example, eastward GWs  
 528 are visible in the upper mesosphere from about  $10^\circ\text{E}$  to  $40^\circ\text{E}$  and from about  
 529  $90^\circ\text{E}$  to  $150^\circ\text{E}$ . When the secondary GWs propagate into the mesopause re-  
 530 gion and lower thermosphere, they become subject to strong refraction by  
 531 the variable vertical wind shears that are induced by the semi-diurnal tide  
 532 and traveling planetary waves. Figure 7a indicates that the secondary GWs  
 533 dissipate in this regime because many of the GW phase lines flatten or be-  
 534 come more horizontal with increasing height for  $z \sim 90 - 120$  km. Since the  
 535 resulting wave-mean flow interactions are expected to be localized in space  
 536 and time, this gives rise to the generation of tertiary GWs. Overall, there  
 537 are mainly higher-order GWs above about  $z \sim 150$  km. These waves have  
 538 very long vertical wavelengths and phase speeds of several  $100 \text{ m s}^{-1}$  (Vadas,  
 539 2007; Vadas and Becker, 2019; Becker and Vadas, 2020), which is much larger  
 540 than what is typical in the wintertime lower and middle atmosphere. Note  
 541 that the phase inclinations of the thermospheric GWs in Fig. 7a do not indi-  
 542 cate clear westward or eastward propagation directions, especially not in the  
 543 longitude sector from about  $30^\circ\text{W}$  to  $60^\circ\text{E}$ .

544 The lower row in Fig. 7 shows the same snapshots as the upper row,  
 545 but during the SSW on 31 January 2017. The wind reversal is indicated by  
 546 the predominantly westward flow in the upper stratosphere and lower meso-  
 547 sphere (colors in panel d). Panel c shows westward and eastward propagating  
 548 primary GWs in the stratosphere. The phase inclinations of these GWs in  
 549 the mesosphere indicate predominantly eastward propagation, as is expected  
 550 due to the predominantly westward large-scale zonal wind. The GWs in the  
 551 stratosphere and mesosphere during the wind reversal have much weaker am-  
 552 plitudes than during the strong vortex period. The primary GWs dissipate  
 553 in the upper mesosphere due to eastward vertical wind shear. Again, this  
 554 process is expected to be localized in space and time, therefore generating  
 555 secondary GWs that propagate to higher altitudes. The phase inclinations  
 556 of these secondary GWs indicate eastward and westward propagation direc-  
 557 tions in the mesopause region and lower thermosphere. Like on December  
 558 27, higher-order GWs having large vertical wavelengths emanate from the  
 559 lower thermosphere. Overall, these GWs have much weaker amplitudes than  
 560 during the strong vortex period. This is consistent with the aforementioned  
 561 correlation between TIDs and the polar vortex when assuming that quiet-

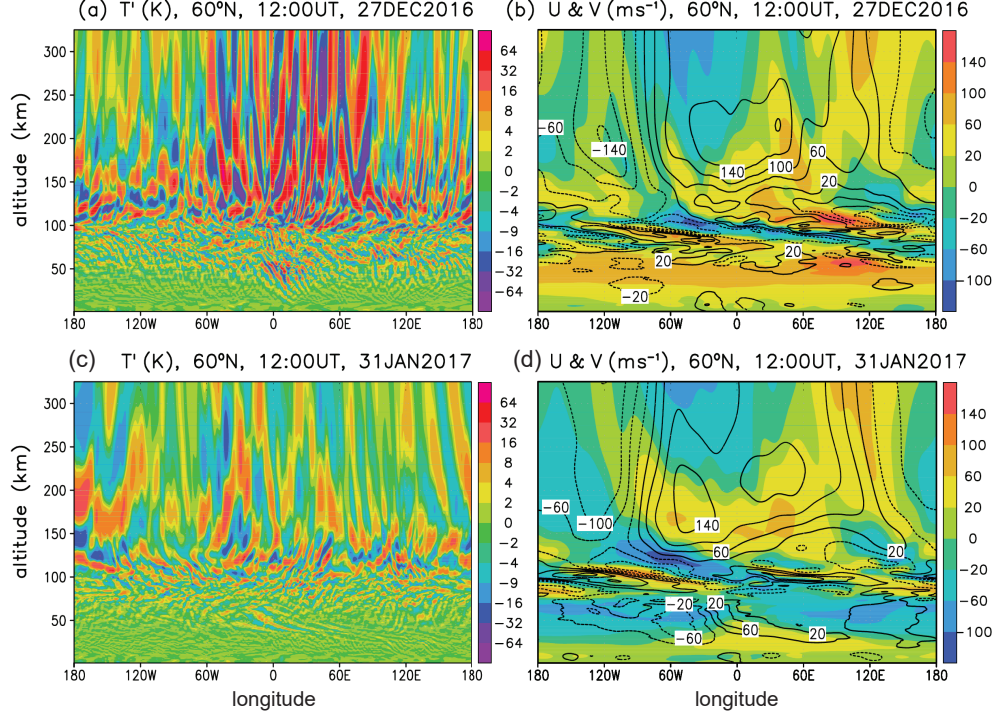


Figure 7: Illustration of MSVC during wintertime as simulated by the HIAMCM. Longitude-height plot of GW temperature perturbations at 60°N on 27 December 2016 (strong vortex) at 12:00 UT. (b) Large-scale zonal wind (colors) and meridional wind (black contours for  $\pm 20, \pm 60, \pm 100, \pm 140, 180 \text{ m s}^{-1}$ ). (c) and (d) Same as (a) and (b), but on 31 January 2017 (SSW). See Becker et al. (2022a) for further details.

time TIDs are driven by GWs from below.

The horizontal structures of the higher-order GWs in the thermosphere are illustrated in Fig. 8 by showing north-polar projections of temperature GW perturbations (colors) and the large-scale horizontal wind (white arrows) at  $z = 250 \text{ km}$ . Assuming that higher-order GWs are generated in the lower thermosphere as concentric ring structures (Vadas and Becker, 2019; Becker et al., 2022a; Vadas et al., 2024), the GW dissipation induced by mainly the diurnal tidal winds leads to partial concentric ring structures at higher altitudes where the largest amplitudes are found for propagation directions that are roughly against the tidal winds. Figure 8a,c indicate three concentric ring structures that are indicative of higher-order GW sources in the lower thermosphere. These sources are located over Scandinavia (visi-

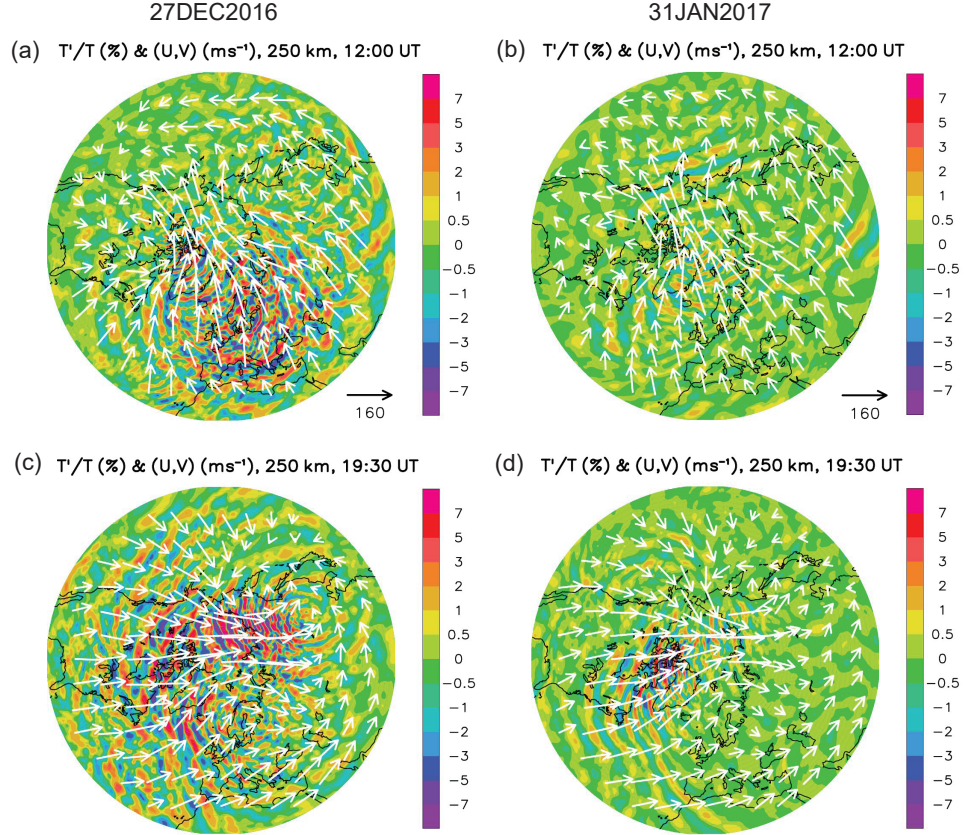


Figure 8: North polar plots of GW temperature perturbations (colors) and the large-scale horizontal wind (white arrows, arrow scale in  $\text{ms}^{-1}$ ) at  $z = 250 \text{ km}$  from the HIAMCM. (a) 27 December 2016, 12 UT. (b) 31 January 2017, 12:00 UT. (c),(d) Same as (a),(b) but at 19:30 UT. See Becker et al. (2022a) for further details.

ble in panel c), over eastern Siberia (visible in panel a and c), and over the Labrador Sea (visible in panel a). The GWs emanating from these sources propagate mainly equatorward during local noon and early afternoon (over Europe at 12 UT and over North America at 19:30 UT) because the tidal winds are poleward and strongest in these regions. During the SSW event on 31 January 2017, the general behavior of the higher-order GWs is qualitatively similar. Their amplitudes, however, are much weaker as a result of much weaker MSVC as discussed above.

Becker et al. (2022a) determined the average daily cycle of GWs in the thermosphere during the strong vortex period by post-processing the model data from 21 to 30 December 2016. They computed averages from 23:30 to 00:30 UT, 05:30 to 06:30 UT, 11:30 to 12:30 UT, and 17:30 to 18:30 UT, taking all 10 days into account and taking advantage of the 10 minute ca-

587 dence of the model output. Figure 9 illustrates the resulting average daily  
 588 cycle in the thermosphere at  $10^{-7}$ hPa ( $z \sim 300$  km) at 0, 6, 12, and 18 UT.  
 589 Colors show the GW kinetic energy per unit mass. The black arrows show  
 590 the large-scale horizontal wind, while the white arrows show the vertical flux  
 591 of horizontal momentum due to GWs. The black arrows confirm the daily  
 592 cycle of the large-scale horizontal wind in the thermosphere that is due to the  
 593 diurnal tide, with cross-polar flow from the dayside to the nightside, which  
 594 facilitates equatorward propagation of higher-order GWs during local noon  
 595 and afternoon (Crowley and Rodrigues, 2012). This average GW propaga-  
 596 tion direction is evident from the momentum flux vectors (white arrows).  
 597 These results reveal a significant daily cycle of the GW amplitudes in the  
 598 winter thermosphere. On average, the GW amplitudes at middle latitudes  
 599 are strongest where and when the tidal flow is strongest, which is the case  
 600 roughly around local time noon and afternoon when the tidal flow has a  
 601 strong poleward component. Furthermore, the GW amplitude maximum ex-  
 602 tends northwestward, that is, to polar latitudes during local morning. Here,  
 603 the tidal wind has a strong westward component such that the GWs in this  
 604 regime exhibit a strong eastward momentum flux. This effect is induced by  
 605 the auroral circulation (Forbes, 2007), which is further discussed in Becker  
 606 et al. (2022a).

607 Figure 10 shows that the simulated GWs in the thermosphere are con-  
 608 sistent with observations. The keogram of GW perturbations from the HI-  
 609 AMCM on 30 Decemeber 2016 (panel a) confirms southward propagating  
 610 GWs at  $z = 300$  km. Corresponding perturbations of the total electron con-  
 611 tent (dTEC) as derived from observations using the Global Navigation Satel-  
 612 lite System (GNSS) on the same day (panel b) show a very similar behavior.  
 613 While there was strong GW and TID activity in late December 2016, these  
 614 variations had much weaker amplitudes during the SSW in late January  
 615 2017, as can be concluded from the simulated GWs and observed dTEC in  
 616 the lower row of Fig. 10. Moreover, the wave characteristics simulated by the  
 617 HIAMCM are very similar to those seen in dTEC. This is indicated in the  
 618 figure by inserting a few phase lines. For case #1 (around local noon on 27  
 619 December 2016), these phase lines correspond to southward propagation with  
 620 a horizontal wavelength of  $\sim 700$  km and a period of  $\sim 45$  minutes, resulting in  
 621 a ground-based horizontal phase speed of  $c_{ph} \sim 270$  m s $^{-1}$ . The case #2 GW  
 622 phases occur shortly after nightfall. Becker et al. (2022a) showed that these  
 623 waves had an approximate southwestward horizontal propagation direction  
 624 and a period of  $\sim 60$  minutes. The apparent horizontal wavelengths in the



21DEC–30DEC2016,  $10^{-7}$ hPa ( $\sim 300$  km):  
 GW kin. energy ( $\text{m}^2\text{s}^{-2}$ ) & (U,V) ( $\text{ms}^{-1}$ ) & GW mom. flux ( $\text{m}^2\text{s}^{-2}$ )

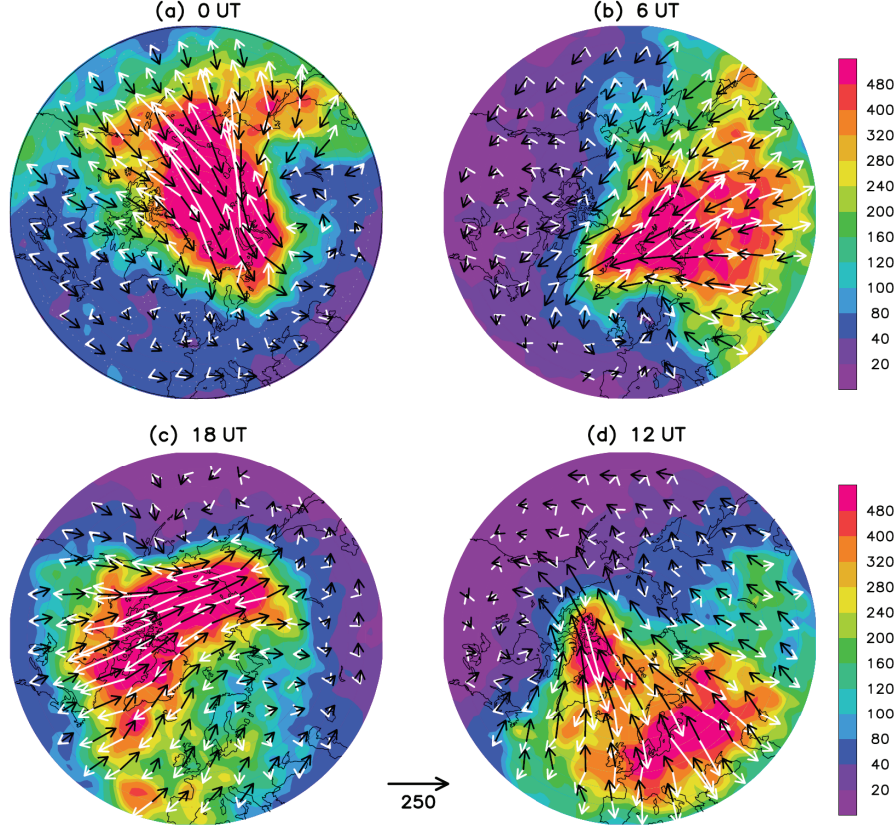


Figure 9: Average daily cycle in the thermosphere during the strong vortex period from 21 to 30 December 2016 at  $10^{-7}$ hPa ( $z \sim 300$  km). Colors show the average GW kinetic energy per unit mass at (a) 0 UT, (b) 6 UT, (c) 18 UT, and (d) 12 UT. The black and white arrows show the corresponding average large-scale horizontal wind and the vertical GW flux of horizontal momentum, respectively. The arrow scale (between panel c and d) is the same for the black and white arrows, but refers to the respective units, that is  $\text{m s}^{-1}$  or  $\text{m}^2\text{s}^{-1}$ . See Becker et al. (2022a) for further details.

625 longitudinal and latitudinal directions were estimated to be 800 and 900 km,  
 626 respectively, yielding a true horizontal wavelength of  $\sim 450$  km and a phase  
 627 speed of  $c_{ph} \sim 130 \text{ m s}^{-1}$ . Such values are typically observed for medium-  
 628 to-large-scale TIDs, even though the simulated wavelengths are somewhat

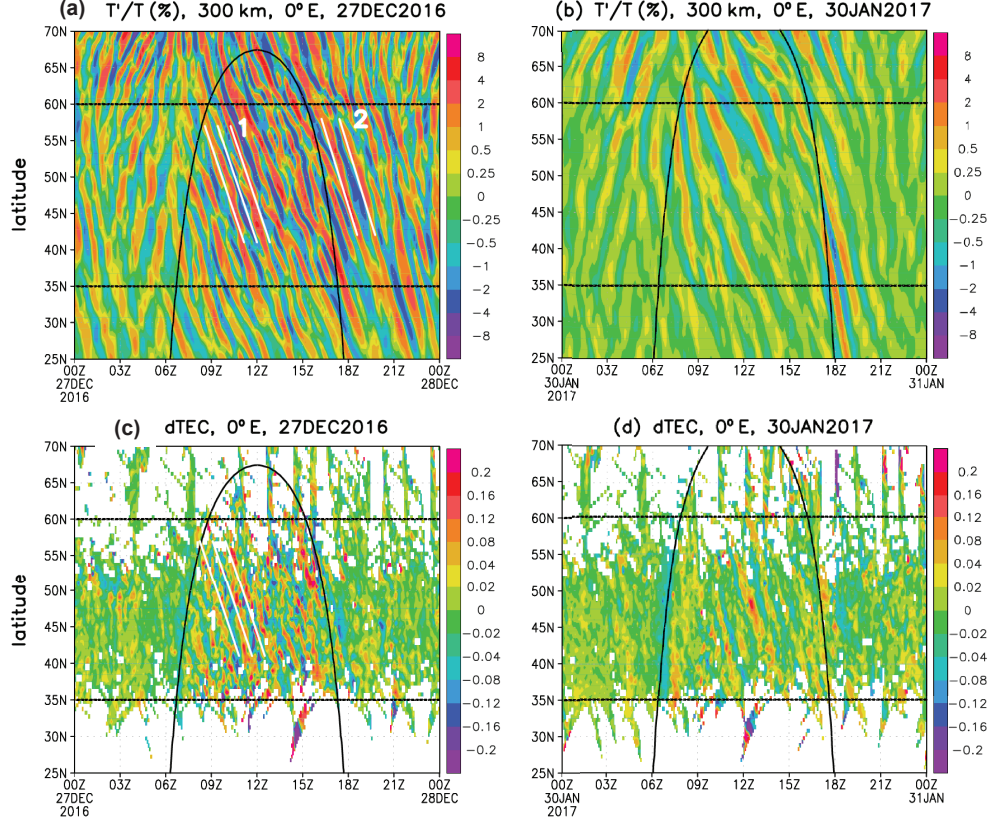


Figure 10: Keograms of the simulated relative temperature perturbations at 300 km height (upper row) and observed dTEC (lower row) at 0°E and from 25°N to 70°N. The left column is for 27 December 2016 (strong vortex) and the right columns is for 30 January 30 (SSW). The straight white lines are inserted to indicate wave phases (see text). Sunrise and sunset are indicated by the curved black lines. See Becker et al. (2022a) for further details.

629 larger than found by Frisell et al. (2016). Figure 10 strongly suggests that  
 630 the observed quiet-time TIDs are driven to a large extent by GWs that result  
 631 from MSVC. Becker et al. (2022a) mentioned that the observed TID activ-  
 632 ity amplified again from about 31 January to 7 February 2017 despite the  
 633 ongoing SSW. This amplification was very likely due to geomagnetic forcing  
 634 ( $K_p=3+$  to  $K_p=5$  during this period). Such an effect was not reflected by  
 635 the GWs simulated by the HIAMCM due to the lack of geomagnetic forcing  
 636 in the model.



Figure 9 implies that there is a strong cancellation of the GW momentum flux and drag contributions from different longitudes in the zonal and temporal mean because of the variations of GW propagation and dissipation induced by the tidal winds. Therefore, a zonal-mean zonal GW drag obscures most of the information about the actual GW-mean flow interactions. Indeed, GW-mean flow interaction in the winter thermosphere is mainly due to GW-tidal interaction. The crucial role of the GW-tidal interactions is also well known for the MLT (e.g. Senf and Achatz, 2011; Becker, 2017; Becker and Vadas, 2018; Heale et al., 2022a; Becker and Oberheide, 2023). Many details of these GW-tidal interactions remain to be understood.

The HIAMCM results presented in Becker et al. (2022a) indicate that the GW drag in the zonal direction is not very relevant in the thermosphere when compared to the contributions from thermal tides and ion drag. Even though community whole-atmosphere models with parameterized GWs do not include MSVC, they also do not predict any notable effect in the thermosphere from parameterized GWs (e.g. Fomichev et al., 2002; Liu et al., 2009; Smith, 2012). The reason is that primary GWs from the mid-latitude troposphere that propagate to the thermosphere are efficiently dissipated by molecular viscosity (Vadas, 2007; Becker and McLandress, 2009). Indeed, the strong EPF divergences simulated in the thermosphere above about 150 km height (see Fig. 5) are mainly due to tides. Nevertheless, the contributions from mainly secondary GWs in the lower thermosphere are still relevant in the zonal mean and contribute to the driving of the reversed residual circulation cells, including their hemispheric difference as discussed in Becker and Oberheide (2023). The diurnal thermal tide in the thermosphere is mainly forced (generated) by solar heating in the  $z \sim 150 - 200$  km height regime (Torr et al., 1981), but in addition by ion drag forcing in the polar regions (Forbes, 2007). The latter effect leads to the eastward EPF divergence in the polar thermosphere in Fig. 5c,d as discussed in Becker et al. (2022a). In addition, the zonal component of the ion drag (white contours in Fig. 5a,c) is the major driver of the summer-to-winter circulation in the upper thermosphere as was recently confirmed by Liu et al. (2024a).

### 5.3. Secondary GWs from the Hunga Tonga-Hunga Ha’apai volcanic eruption

Even the highest resolutions currently feasible in GW-resolving whole-atmosphere models are not sufficient to simulate the primary GWs from deep convection or volcanic eruptions. If MSVC from such primary GWs needs to be taken into account, the localized and intermittent ambient-flow effects that

674 generate secondary GWs at higher altitudes need to be precalculated by other  
675 means and then implemented into the global model. Vadas et al. (2023b,c)  
676 and Huba et al. (2023) performed these precalculations of small-scale, high-  
677 frequency GWs using a combination of tools that is called the Model for  
678 gravity wavE SOurce, Ray trAcing and reConstruction (MESORAC).

679 The MESORAC was applied to simulate the thermospheric and iono-  
680 spheric disturbances caused by the eruption of the Hunga Tonga-Hunga  
681 Ha’apai (hereafter: Tonga) volcanic eruption on 15 January 2022. To this  
682 end, the primary GWs from the Tonga event were inferred from the updrafts  
683 in the stratosphere and mesosphere as observed by NOAA’s Geostationary  
684 Operational Environmental Satellite (GOES). These GWs were ray-traced  
685 forward in time, and the GW field was reconstructed using the GW phases  
686 and the GW dissipative dispersion and polarization relations. The back-  
687 ground atmosphere for this ray-tracing computation was taken from the HI-  
688 AMCM simulation for 15 January 2022 without any perturbations related to  
689 the Tonga event (“no-Tonga” run). The ray-traced primary GWs dissipated  
690 from both saturation and molecular viscosity. This resulted in very strong  
691 LBFs (and heatings). We obtained localized and intermittent accelerations  
692 of more than  $1 \text{ ms}^{-2}$ . The majority of these effects occurred about 30-90  
693 minutes after the major eruption and were confined to the geographical re-  
694 gion around the volcano. That is, the primary GWs from the Tonga event  
695 could not account directly for any of the far-field effects that were observed  
696 around the globe after the volcanic eruption. The HIAMCM simulation of  
697 the January 15-19 period was then repeated with the precalculated LBFs  
698 and heatings from MESORAC (“Tonga” run). The HIAMCM responded  
699 with a broad spectrum of large-amplitude, high-phase-speed secondary GWs  
700 that propagated around the globe for several days in the thermosphere. Fig-  
701 ure 11a shows an example of a LBF from the dissipation of primary GWs  
702 computed with the MESORAC. Note that this LBF occurred at about 5:30  
703 UT in the lower thermosphere only a few hundred kilometers away from the  
704 volcano and about one hour after the first eruption. Such LBFs generated  
705 secondary GWs in the HIAMCM. Figure 11b shows a snapshot of these sec-  
706 ondary GWs in terms of the vertical wind at 280 km and 12:00 UT on 15  
707 January 2022.

708 These secondary GWs can be compared to satellite observations of winds  
709 by ICON-MIGHTI (Harding et al., 2017; Immel et al., 2018). Figure 12  
710 shows the ICON-MIGHTI zonal winds over the eastern Pacific, North Amer-  
711 ica, and the Atlantic Ocean. These winds display the GWs from Tonga

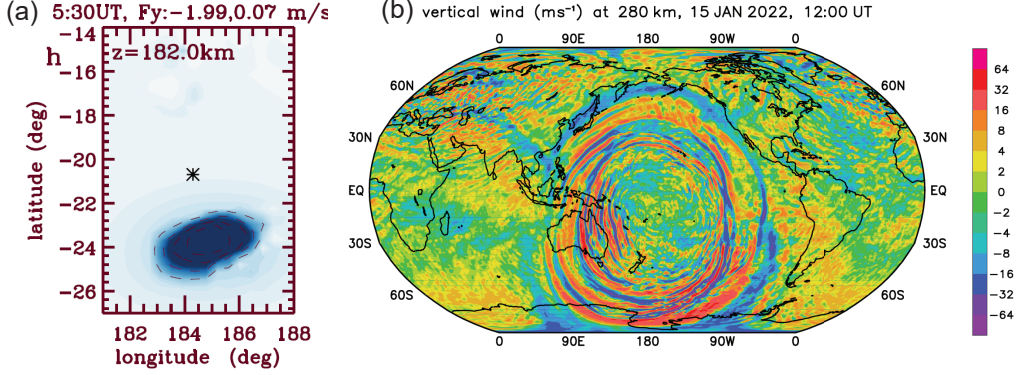


Figure 11: (a) Example of a southward local body force (LBF) at  $z=182$  km and 05:30 UT on January 15, 2022. Such LBFs were computed with the MESORAC from the dissipation of primary GWs that were generated by the updrafts from the Tonga volcanic eruption (which primarily occurred from about 04:15 to 05:50 UT). (b) Snapshot of the secondary GWs simulated by the HIAMCM in terms of the vertical wind at  $z=280$  km and 12:00 UT. See Vadas et al. (2023b) for further details.

712 during four consecutive orbits. The left column shows the tangent longitude  
 713 versus latitude and time during these orbits. The right column shows the  
 714 measured zonal winds. We included pink vertical lines that mark the lo-  
 715 cations of disturbances that would have propagated from the region of the  
 716 Tonga eruption with various horizontal phase speeds. Overall these plots in-  
 717 dicate that the GWs from Tonga had very large amplitudes, large scales,  
 718 and horizontal phase speeds of  $100$  to  $600 \text{ ms}^{-1}$ . Figure 13 compares the  
 719 analyzed ICON-MIGHTI zonal winds with HIAMCM zonal winds sampled  
 720 along the same orbits. Direct comparisons showed that the timing and the  
 721 amplitudes of the HIAMCM zonal wind perturbations agree reasonably well  
 722 with ICON-MIGHTI (Vadas et al., 2023b). To achieve the best agreement,  
 723 however, we extracted the zonal wind perturbation amplitudes related to  
 724 the Tonga eruption by computing the difference between the Tonga run and  
 725 the no-Tonga run, and then multiplied these wind perturbations by a factor  
 726 of  $1.5$ . The “scaled Tonga wind” is given by the no-Tonga winds plus the  
 727 scaled perturbations. In the right column of Fig. 13 we plot these model data  
 728 30 minutes later than the satellite data. Eastward and upward-propagating  
 729 GWs are observed west of  $0^\circ\text{E}$  on the dayside. The along-track wavelengths  
 730 increase with distance from Tonga, as is expected for GWs generated by a  
 731 point source. In addition, the GWs in each successive orbit have smaller

732 amplitudes and smaller phase speeds, which is expected as well.

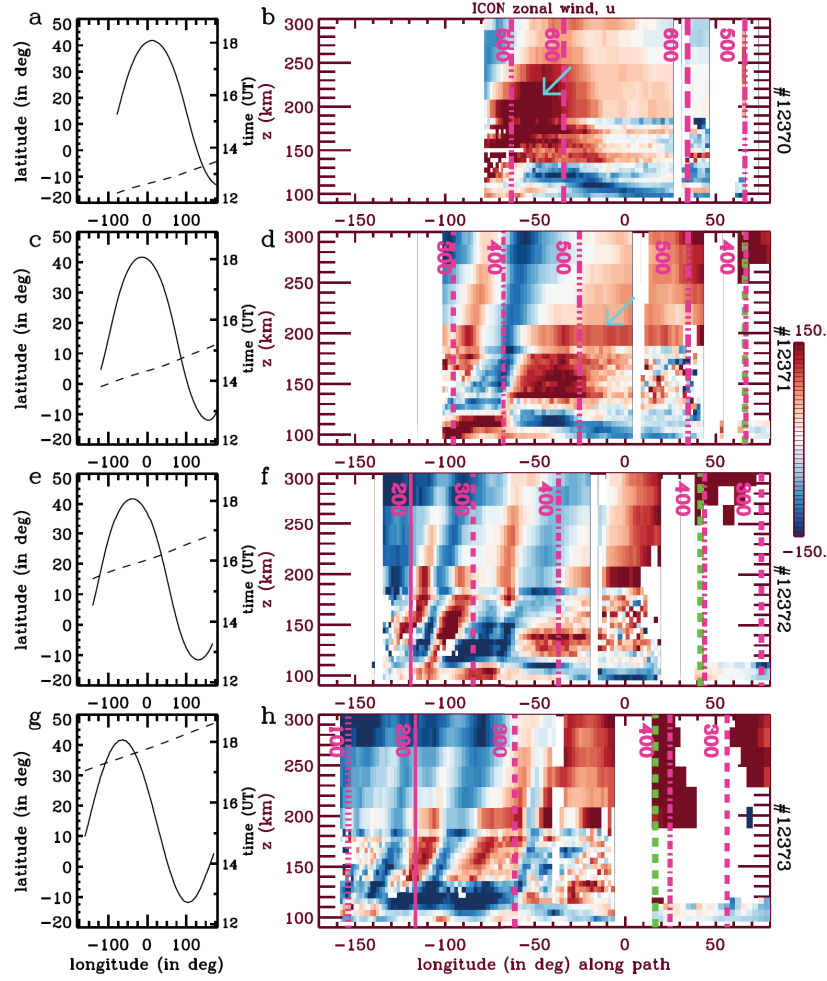


Figure 12: (a) ICON-MIGHTI tangent longitude versus latitude (solid line, left y-axis) and tangent longitude versus time (dashed line, right y-axis) for orbit #12370 on 15 January 2022. (b) ICON-MIGHTI zonal wind as a function of the tangent longitude for orbit #12370. Rows 2-4: Same as row 1 but for orbits #12371, 12372 and 12373. The vertical pink lines show the locations of waves that originated in the thermosphere above Tonga at 5:00 UT with horizontal phase speeds of 100, 200, 300, 400, 500, and 600  $\text{m s}^{-1}$ , as labelled. Phase-speed lines are not shown where the westward and eastward waves from Tonga would overlap. Turquoise arrows indicate the fastest large-scale secondary GWs with horizontal phase speeds larger than 500  $\text{m s}^{-1}$ . Green-dashed lines show the solar (sunset) terminator. From Vadas et al. (2023b).

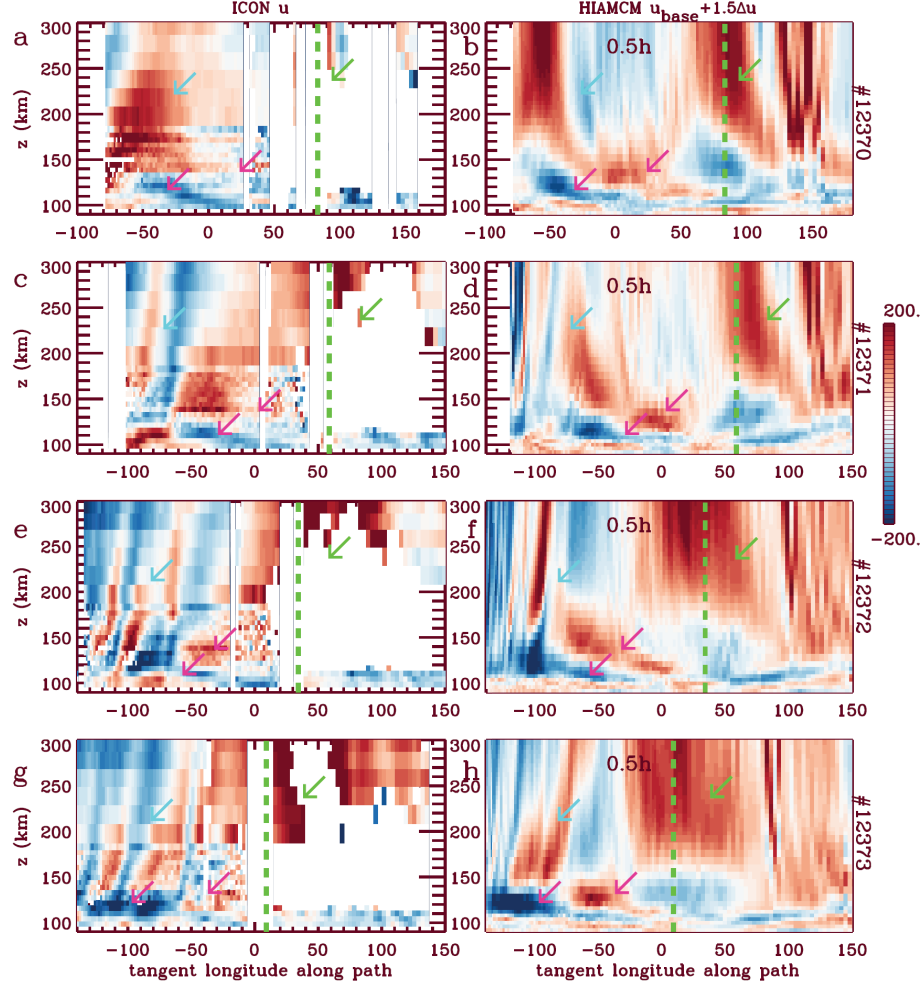


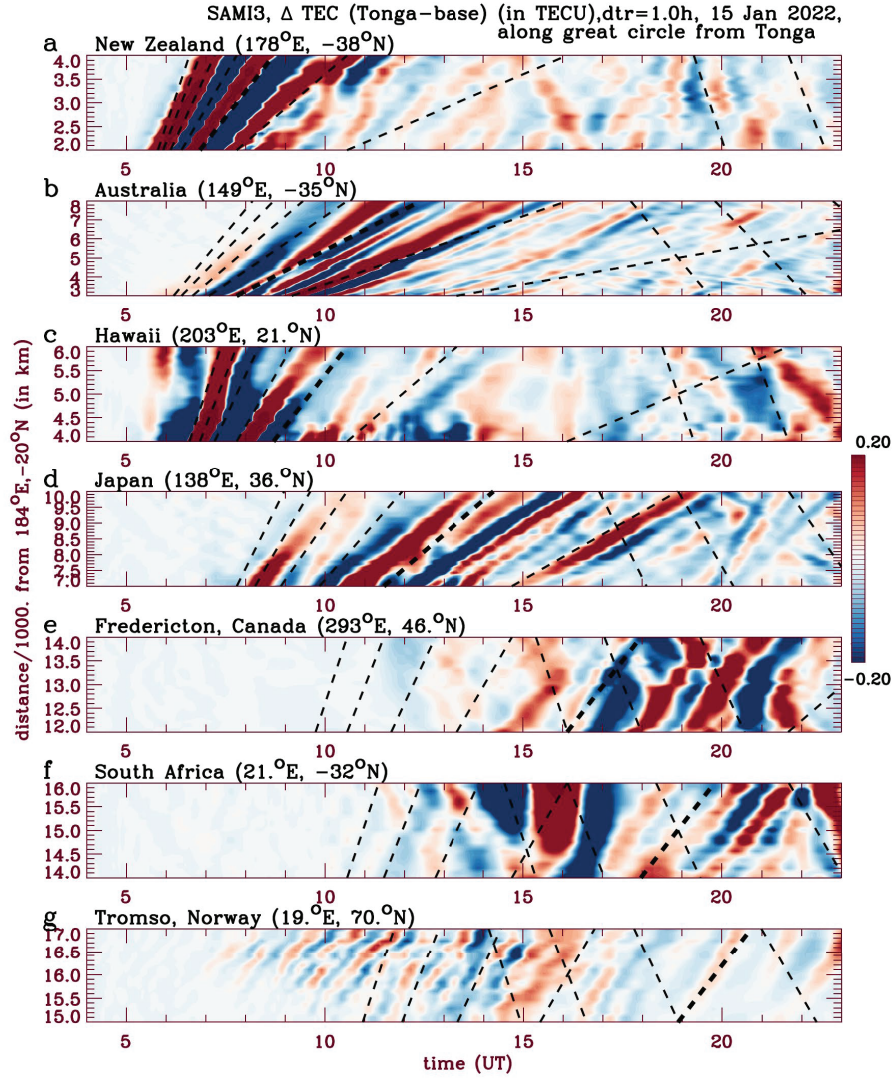
Figure 13: (a),(c),(e),(g) Zonal winds measured by ICON as functions of the tangent longitude and height  $z$  for orbits #12370, 12371, 12372, and 12373, respectively. (b),(d),(f),(h) HIAMCM zonal winds from the no-Tonga run plus 1.5 times the perturbation from the Tonga minus the no-Tonga run as functions of the tangent longitude and  $z$  and sampled 30 minutes later than the ICON times for orbits #12370, 12371, 12372 and 12373, respectively. The HIAMCM winds are smoothed over 200 km horizontally prior to sampling. The green dashed lines show the sunset solar terminator. Turquoise, pink and green arrows indicate the Tonga GWs, the tides, and the terminator waves, respectively. These arrows are in the same locations in each row. From Vadas et al. (2023b, their Fig. 5).

733 Summarizing, the ICON-MIGHTI instrument observed northeastward-  
 734 propagating secondary GWs from Tonga having horizontal phase speeds of  
 735 about 100 to 600  $\text{m s}^{-2}$  and horizontal wavelengths of about 800 to 7500 km,  
 736 which is in good agreement with the model results. Also the timing and the

737 very large amplitudes of the observed waves are in reasonable agreement with  
 738 the model. Thus, these observations provide excellent confirmation that the  
 739 LBF mechanism applies as an explanation for the (secondary) GWs from the  
 740 Tonga eruption.

741 To further validate the HIAMCM simulation of the secondary thermo-  
 742 spheric GWs from the Tonga event, the model output was used to drive the  
 743 SAMI3 ionospheric model (Huba et al., 2023). The keograms of the dTEC  
 744 as simulated by the SAMI3 (Vadas et al., 2023c) were similar to those pub-  
 745 lished by Themens et al. (2022). These authors analyzed the dTEC for a  
 746 number of regions and computed keograms of the dTEC along great circles  
 747 from Tonga through these regions (Themens et al., 2022, their Fig. 4). They  
 748 used a detrend window of 30 minutes for this analysis. Vadas et al. (2023c)  
 749 revisited these data and used a detrend window of 1 hr to better emphasize  
 750 the larger-scale secondary GWs (see Fig. 7 in that study). The model output  
 751 from the SAMI3 was then analyzed in the same way and the result is shown  
 752 here in Fig. 14. Vadas et al. (2023c) found that the SAMI3 reproduced the  
 753 GNSS dTEC observations very well. This holds particularly for the wave  
 754 periods and for the different arrival times of the wave perturbations in dif-  
 755 ferent regions. Figure 14 also shows that the secondary GWs with longer  
 756 periods arrive first, implying that these waves have larger horizontal phase  
 757 speeds and larger vertical group velocities. This feature of the secondary  
 758 GWs is typical for a GW spectrum initiated by the LBF mechanism (Vadas  
 759 et al., 2018; Vadas and Becker, 2019), which is another confirmation that this  
 760 mechanism gives a consistent picture for the wave perturbations in the ther-  
 761 mosphere that were caused by the Tonga volcanic eruption. Note that the  
 762 fastest (longest-period) secondary FWs were also observed to have decreased  
 763 the F region peak by  $\sim 120$  km over the western US (Vadas et al., 2023c).

764 Alternative attempts to explain the wave perturbations in the thermo-  
 765 sphere from the Tonga event proposed that the observations were due to  
 766 Lamb waves or Lamb waves leaking into the thermosphere as GWs (e.g.  
 767 Zhang et al., 2022; Liu et al., 2023). Vadas et al. (2023c) showed that such  
 768 an interpretation is inconsistent with the observations, especially with those  
 769 very-large-amplitude GWs that were observed worldwide and had horizontal  
 770 phase speeds  $> 300 \text{ m s}^{-1}$ . On the other hand, MSVC as simulated by our  
 771 combination of models explains most observations reasonably well and in a  
 772 dynamically consistent fashion.





## 773 6. Summary and some open questions

774 We reviewed the multi-step vertical coupling (MSVC) due to GWs and  
 775 the relevance of this mechanism to the general circulation and to GWs in the  
 776 upper mesosphere and thermosphere/ionosphere. At the heart of MSVC is  
 777 the local body-force (LBF) mechanism according to which the localized (in  
 778 space and time) breaking or dissipation of GW packets leads to imbalances  
 779 in the ambient flow which in turn result in the generation of new (secondary  
 780 or higher-order) GWs (Vadas and Fritts, 2002; Vadas et al., 2003, 2018). We  
 781 distinguished this GW generation from the energy cascade associated with  
 782 GW breaking that is characterized by energy and momentum flux transfer to  
 783 smaller and smaller scales. We argued that small-scale, high-frequency GWs  
 784 observed in the middle atmosphere that are subject to the universal behav-  
 785 ior of GW spectra (energy spectra with spectral slopes of  $m^{-3}$  and  $\omega^{-2}$  to  
 786  $\omega^{-5/3}$  with regard to the vertical wavenumber and frequency, respectively),  
 787 are likely a reflection of stratified macro-turbulence (SMT) that is main-  
 788 tained by the instability and breaking of incident GW packets. We showed  
 789 that observed vertical wavenumber, horizontal wavenumber, and frequency  
 790 spectra of GWs are all consistent with such a macro-turbulent inertial range  
 791 on average for small-enough scales and periods. Note, however, that high-  
 792 frequency primary GWs from deep moist convection or volcanic eruptions do  
 793 not fit into this category. Such primary GWs often have long vertical wave-  
 794 lengths and correspondingly large vertical group velocities so that they can  
 795 propagate to the mesosphere or thermosphere before becoming unstable or  
 796 being dissipated directly by molecular viscosity (Vadas, 2007; Vadas and Liu,  
 797 2013; Vadas et al., 2014). It is an ongoing research question as to whether  
 798 primary or secondary GWs from deep moist convection play the major role  
 799 for GWs/TIDs in the thermosphere/ionosphere above regions of deep moist  
 800 convection (see Vadas and Azeem, 2021; Heale et al., 2022b).

801 We presented a number of examples of MSVC that were simulated with  
 802 the High Altitude Mechanistic general Circulation Model (HIAMCM) and a  
 803 former model version, and which were compared to observations for valida-  
 804 tion. According to MSVC, the observed large-amplitude GWs in the winter  
 805 mesopause region at middle to high latitudes (e.g., Chen et al., 2016) are sec-  
 806 ondary GWs that are generated around and above the wind maximum of the  
 807 polar night jet. Importantly, these secondary GWs are eastward propagating  
 808 in the winter mesopause region (Becker and Vadas, 2018) and are essential  
 809 for understanding the observed prevailing winds in the winter mesosphere



810 and lower thermosphere (Hindley et al., 2022). To date, only GW-resolving  
811 models can simulate these GWs and their eastward GW drag in the win-  
812 ter mesopause region. Furthermore, the eastward secondary GW drag is  
813 stronger for a stronger polar vortex (Vadas and Becker, 2019; Becker et al.,  
814 2022a; Harvey et al., 2022).

815 The dissipation of the wintertime secondary GWs in the strong wind  
816 shears associated with thermal tides and traveling planetary waves in the  
817 lower thermosphere leads to the generation of tertiary (higher-order) GWs,  
818 which again can be understood by the LBF mechanism (Vadas and Becker,  
819 2019; Vadas et al., 2023a, 2024). Therefore, GWs in the winter thermo-  
820 sphere are mainly higher-order GWs. Model results show that these GWs  
821 undergo a strong daily cycle, with GW amplitudes being maximum on av-  
822 erage around local noon and early afternoon at F region altitudes (Becker  
823 et al., 2022a). These wintertime GWs propagate equatorward (against the  
824 tidal flow), confirming that most of the quiet-time traveling ionospheric dis-  
825 turbances (TIDs) during the daytime are driven by GWs from below. In con-  
826 trast to conventional wisdom, however, the GWs that drive wintertime TIDs  
827 are by no means primary GWs from the troposphere, but are higher-order  
828 GWs resulting from MSVC. Moreover, since the generation of secondary and  
829 higher-order GWs is correlated with the strength of the polar vortex (Vadas  
830 and Becker, 2019), MSVC also explains why the strength of observed quiet-  
831 time TIDs is correlated with the strength of the polar vortex (Frissell et al.,  
832 2016; Nayak and Yigit, 2019; Becker et al., 2022a).

833 Global-modeling studies of MSVC from deep moist convection were per-  
834 formed by Vadas and Liu (2009, 2013) and Vadas et al. (2014). These studies  
835 used a global model with an effective horizontal resolution  $\lambda_h \sim 2000\text{--}3000$  km  
836 to simulate large-scale secondary GWs from deep convection. However,  
837 medium-scale secondary GWs should also have been generated, as was shown  
838 by reverse ray-tracing (Vadas and Crowley, 2010), which then would have  
839 induced medium-scale TIDs. These earlier model studies remain to be re-  
840 visited using a global model with high-enough effective resolution to capture  
841 all the relevant secondary GWs. The HIAMCM or the latest version of the  
842 Whole Atmosphere Community Climate Model with ionosphere eXtension  
843 (WACCM-X) (Liu et al., 2024b) would be such global model candidates. In  
844 principle, the generation of primary GWs by deep moist processes is explic-  
845 itly included in such models (e.g. Liu et al., 2014). However, since these  
846 models cannot adequately resolve this process due to insufficient resolution,  
847 the explicitly simulated MSVC from parameterized deep moist convection

848 is not expected to be realistic as compared to what has been achieved for  
849 wintertime conditions for the primary GWs from jets and fronts, flow over  
850 topography, and the polar vortex (e.g. Becker et al., 2022b; Vadas et al.,  
851 2023a, 2024).

852 To adequately include the primary and secondary GWs from deep moist  
853 convection in a GW-resolving whole-atmosphere models, such models need  
854 to be coupled to local convection models like the Model for gravity wave  
855 Source, Ray tracing and reConstruction (MESORAC). The GWs from both  
856 models then need to be coupled to an ionospheric model (SAMI3) to elu-  
857 cidate the effects of MSVC from deep moist convection on the thermo-  
858 sphere/ionosphere. In this paper we reviewed simulation results where the  
859 MESORAC model suite was applied to compute the primary GWs and LBFs  
860 in the middle and upper atmosphere that were generated by the Tonga vol-  
861 canic eruption on 15 January 2022. The LBFs were used to perturb the HI-  
862 AMCM to simulate the secondary GWs induced by the Tonga event (Vadas  
863 et al., 2023b). The HIAMCM output was furthermore used to drive the iono-  
864 spheric model SAMI3 to simulate the corresponding ionospheric disturbances  
865 (e.g. Huba et al., 2023). These model results showed very good agreement  
866 with satellite and GNSS observations of thermospheric waves and ionospheric  
867 disturbances caused by the Tonga event, thereby validating the coupling of  
868 the three models. A full coupling of the MESORAC to a whole-atmosphere  
869 model to simulate MSVC from deep moist convection routinely is yet to be  
870 developed. Such a coupled model would be particularly useful to investi-  
871 gate the role of MSVC in the tropics, as well as from subtropical to middle  
872 latitudes during summertime.

873 The simulation of MSVC in high-resolution models needs to be further  
874 improved in several ways. For example, Chu et al. (2022) analyzed lidar data  
875 in the southern winter MLT and discovered upward GW heat (temperature)  
876 flux in a layer around  $\sim 97$ -106 km. Such a flux cannot exist when GWs are  
877 considered in the anelastic approximation, where the heat flux is either zero  
878 in the conservative case or downward in the case of thermal dissipation (e.g.,  
879 Becker, 2017). On the other hand, when taking the fully compressible polar-  
880 ization relations of Vadas (2013, Appendix B) into account, upward (down-  
881 ward) conservatively propagating GWs possess an upward (downward) heat  
882 flux. The upward heat flux observed by Chu et al. (2022) was presumably due  
883 to upward propagating secondary GWs. This newly discovered phenomenon  
884 of MSVC remains to be simulated with GW-resolving circulation models.  
885 Regarding current community whole-atmosphere models with parameterized

886 GWs we note that these models cannot simulate MSVC at all. The reason  
 887 is that all routinely used conventional GW schemes are based on the single-  
 888 column and steady-state approximation which exclude MSVC by definition  
 889 (see discussions in Becker and Vadas, 2020; Achatz et al., 2024). New GW  
 890 schemes that relax these strong assumptions (e.g. Bölöni et al., 2021) may  
 891 be extended by MSVC in the future. We finally note that the details of the  
 892 simulated MSVC in a GW-resolving model depend crucially on the subgrid-  
 893 scale (SGS) diffusion scheme. The HIAMCM employs a Smagorinsky-type  
 894 diffusion scheme (Becker and Vadas, 2020, Appendix A). Even though this  
 895 scheme can be considered as a physics-based SGS model and is therefore  
 896 an improvement compared to adhoc numerical damping methods, it violates  
 897 the scale-invariance constraint. Scale invariance should be fulfilled by any  
 898 SGS model when the resolved flow is truncated in a macro-turbulent inertial  
 899 range (e.g. Schaefer-Rolffs et al., 2014; Schaefer-Rolffs and Becker, 2018, see  
 900 also references therein). Improved methods should therefore be based on the  
 901 so-called dynamic Smagorinsky model as discussed in Becker et al. (2023).  
 902 Corresponding progress in model development and ongoing improvements in  
 903 computer technology are expected to allow for new insight into MSVC and  
 904 its relevance to the dynamics in the middle and upper atmosphere.

905 **Acknowledgments:** EB was supported by NASA grants 80NSSC22K0174,  
 906 80NSSC19K0834, and 80NSSC21M0180. SLV was supported by NSF grant  
 907 2329957 and by NASA grant 80NSSC24K0274. The McMurdo lidar project  
 908 was supported by NSF grant OPP-2110428, and XC was in part supported  
 909 by AGS-2330168. We are indebted to the editor Ruth Lieberman and to our  
 910 collaborators from the previous studies that gave rise to this review paper.

## 911 **References**

- 912 Achatz, U., 2007a. Gravity-wave breaking: Linear and primary nonlinear  
 913 dynamics. *Adv. Space Res.* 40, 719–733. doi:10.1016/j.asr.2007.03.078.  
 914 Achatz, U., 2007b. Modal and nonmodal perturbations of monochromatic  
 915 high-frequency gravity waves: Primary nonlinear dynamics. *J. Atmos. Sci.*  
 916 64, 1977–1994. doi:10.1175/JAS3940.1.  
 917 Achatz, U., 2007c. The primary nonlinear dynamics of modal and nonmodal  
 918 perturbations of monochromatic inertia-gravity waves. *J. Atmos. Sci.* 64,  
 919 74–95. doi:10.1175/JAS3827.1.

920 Achatz, U., Alexander, M.J., Becker, E., Chun, H.Y., Dörnbrack, A.,  
921 Holt, L., Plougonven, R., Polichtchouk, I., Sato, K., Sheshadri, A.,  
922 Stephan, C.C., van Nierkerk, A., Wright, C.J., 2024. Atmospheric grav-  
923 ity waves: Processes and parameterization. *J. Atmos. Sci.* 81, 237–262.  
924 doi:10.1175/JAS-D-23-0210.1.

925 Avsarkisov, V., Becker, E., Renkowitz, T., 2022. Turbulent coherent  
926 structures in the middle atmosphere: Theoretical estimates deduced  
927 from a gravity-wave resolving general circulation model. *J. Atmos. Sci.*  
928 doi:org/10.1175/JAS-D-21-0005.1.

929 Becker, E., 2009. Sensitivity of the upper mesosphere to the Lorenz  
930 energy cycle of the troposphere. *J. Atmos. Sci.* 66, 648–666.  
931 doi:10.1175/2008JAS2735.1.

932 Becker, E., 2012. Dynamical control of the middle atmosphere. *Space Sci.*  
933 *Rev.* 168, 283–314. doi:10.1007/s11214-011-9841-5.

934 Becker, E., 2017. Mean-flow effects of thermal tides in the mesosphere and  
935 lower thermosphere. *J. Atmos. Sci.* 74, 2043–2063. doi:10.1175/JAS-D-16-  
936 0194.1.

937 Becker, E., Burkhardt, U., 2007. Nonlinear horizontal diffusion for GCMs.  
938 *Mon. Wea. Rev.* 135, 1439–1454. doi:10.1175/MWR3348.1.

939 Becker, E., Garcia, R., Pedatella, N., Vadas, S., Yudin, V., 2023. Explicit  
940 simulation of gravity waves in whole atmosphere models. *Bulletin of the*  
941 *AAS* 55. <https://baas.aas.org/pub/2023n3i027>.

942 Becker, E., Goncharenko, L., Harvey, V.L., Vadas, S.L., 2022a. Multi-step  
943 vertical coupling during the January 2017 sudden stratospheric warming.  
944 *J. Geophys. Res. Space Phys.* 127. doi:10.1029/2022JA030866.

945 Becker, E., Grygalashvyly, M., Sonnemann, G.R., 2020. Gravity wave mix-  
946 ing effects on the OH\*-layer. *Advances in Space Research* 65, 175–188.  
947 doi:10.1016/j.asr.2019.09.043.

948 Becker, E., McLandress, C., 2009. Consistent scale interaction of gravity  
949 waves in the doppler spread parameterization. *J. Atmos. Sci.* 66, 1434–  
950 1449. doi:10.1175/2008JAS2810.1.

- 951 Becker, E., Oberheide, J., 2023. Unexpected DE3 tide in the southern sum-  
 952 mer mesosphere. *Geophys. Res. Lett.* 50. doi:10.1029/2023GL104368.
- 953 Becker, E., Vadas, S.L., 2018. Secondary gravity waves in the winter meso-  
 954 sphere: Results from a high-resolution global circulation model. *J. Geo-  
 955 phys. Res. Atmos.* 123. doi:10.1002/2017JD027460.
- 956 Becker, E., Vadas, S.L., 2020. Explicit global simulation of grav-  
 957 ity waves in the thermosphere. *J. Geophys. Res. Space Phys.*  
 958 doi:10.1029/2020JA028034.
- 959 Becker, E., Vadas, S.L., Bossert, K., Harvey, V.L., Zülicke, C., Hoffmann, L.,  
 960 2022b. A high-resolution whole-atmosphere model with resolved gravity  
 961 waves and specified large-scale dynamics in the troposphere and strato-  
 962 sphere. *J. Geophys. Res. Atmos.* 127. doi:10.1029/2021JD035018.
- 963 Bölöni, G., Kim, Y.H., Borchert, S., Achatz, U., 2021. Toward transient  
 964 subgrid-scale gravity wave representation in atmospheric models. part i:  
 965 Propagation model including nondissipative wave-mean-flow interactions.  
 966 *J. Atmos. Sci.* 78, 1317–1338. doi:10.1175/JAS-D-20-0065.1.
- 967 Brune, S., Becker, E., 2013. Indications of stratified turbulence in a mecha-  
 968 nistic GCM. *J. Atmos. Sci.* 70, 231–247. doi:10.1175/JAS-D-12-025.1.
- 969 Chen, C., Chu, X., 2017. Two-dimensional Morlet wavelet transform and its  
 970 application to wave recognition methodology of automatically extracting  
 971 two-dimensional wave packets from lidar observations in Antarctica. *J.  
 972 Atmos. Sol.-Terr. Phys.* doi:10.1016/j.jastp.2016.10.016.
- 973 Chen, C., Chu, X., McDonald, A.J., Vadas, S.L., Yu, Z., Fong, W., Lu, X.,  
 974 2013. Inertia-gravity waves in antarctica: A case study using simultaneous  
 975 lidar and radar measurements at McMurdo/Scott Base (77.8°S, 166.7°E).  
 976 *J. Geophys. Res.* 118. doi:10.1002/jgrd.50318.
- 977 Chen, C., Chu, X., Zhao, J., Roberts, B.R., Yu, Z., Fong, W., Lu, X., Smith,  
 978 J.A., 2016. Lidar observations of persistent gravity waves with periods  
 979 of 3–10 h in the Antarctic middle and upper atmosphere at McMurdo  
 980 (77.83°S, 166.67°E). *J. Geophys. Res. Space Physics* 121, 1483–1502.  
 981 doi:10.1002/2015JA022127.

- 982 Chu, X., Gardner, C.S., Li, X., Lin, C.Y.T., 2022. Vertical transport of sen-  
983 sible heat and meteoric Na by the complete temporal spectrum of gravity  
984 waves in the MLT above McMurdo (77.84°S, 166.69°E), Antarctica. *J.*  
985 *Geophys. Res. Atmos.* 127. doi:10.1029/2021JD035728.
- 986 Chu, X., Yu, Z., Gardner, C.S., Chen, C., Fong, W., 2011. Lidar observations  
987 of neutral Fe layers and fast gravity waves in the thermosphere (110-155  
988 km) at McMurdo (77.8°s, 166.7°e), Antarctica. *Geophys. Res. Lett.* 38.  
989 doi:10.1029/2011GL050016.
- 990 Chu, X., Zhao, J., Lu, X., Harvey, V.L., Jones, R.M., Becker, E., Chen,  
991 C., Fong, W., Yu, Z., Roberts, B.R., Dörnbrack, A., 2018. Lidar ob-  
992 servations of stratospheric gravity waves from 2011 to 2015 at McMurdo  
993 (77.84°S, 166.69°E), Antarctica: 2. Potential energy densities, lognor-  
994 mal distributions, and seasonal variations. *J. Geophys. Res. Atmos.* 123.  
995 doi:10.1029/2017JD027386.
- 996 Crowley, G., Rodrigues, F.S., 2012. Characteristics of traveling ionospheric  
997 disturbances observed by the TIDDBIT sounder. *Radio Science* 47.  
998 doi:10.1029/2011RS004959.
- 999 Dong, W., Fritts, D.C., Lund, T.S., Wieland, S.A., Zhang, S., 2020. Self-  
1000 acceleration and instability of gravity-wave packets: 2. Two-dimensional  
1001 packet propagation, instability dynamics, and transient flow responses. *J.*  
1002 *Geophys. Res. Atmos.* doi:10.1029/2019JD030691.
- 1003 Fomichev, V.I., Ward, W.E., Beagley, S.R., McLandress, C., McConnell,  
1004 J.C., McFarlane, N.A., Shepherd, T.G., 2002. Extended Cana-  
1005 dian Middle Atmosphere Model: Zonal-mean climatology and phys-  
1006 ical parameterizations. *J. Geophys. Res.* 107, ACL9–1–ACL9–14.  
1007 doi:10.1029/2001JD000479.
- 1008 Forbes, J.M., 2007. Dynamics of the thermosphere. *J. Met. Soc. Japan* 85B,  
1009 193–213.
- 1010 Frissell, N.A., Baker, J.B.H., Ruohoniemi, J.M., Greenwald1, R.A., Ger-  
1011 rard, A.J., Miller, E.S., West, M.L., 2016. Sources and characteris-  
1012 tics of medium-scale traveling ionospheric disturbances observed by high-  
1013 frequency radars in the north american sector. *J. Geophys. Res. Space*  
1014 *Physics* 121, 3722–3739. doi:10.1002/2015JA022168.

1015 Fritts, D.C., Alexander, M.J., 2003. Gravity wave dynamics and effects in  
1016 the middle atmosphere. *Rev. Geophys.* 41. doi:10.1029/2001/RG000106.

1017 Fritts, D.C., Dong, W., Lund, T.S., Wieland, S.A., Laughman, B., 2020.  
1018 Self-acceleration and instability of gravity wave packets: 3. Three-  
1019 dimensional packet propagation, secondary gravity waves, momentum  
1020 transport, and transient mean forcing in tidal winds. *J. Geophys. Res.*  
1021 *Atmos.* doi:10.1029/2019JD030692.

1022 Guo, Y., Liu, A.Z., Gardner, C.S., 2017. First Na lidar measure-  
1023 ments of turbulence heat flux, thermal diffusivity, and energy dissipa-  
1024 tion rate in the mesopause region. *Geophys. Res. Lett.* 44, 5782–5790.  
1025 doi:10.1002/2017GL073807.

1026 Harding, B.J., Makela, J.J., Englert, C.R., Marr, K.D., Harlander, J.M.,  
1027 England, S.L., Immel, T.J., 2017. The MIGHTI wind retrieval al-  
1028 gorithm: Description and verification. *Space Sci. Rev.* 212, 585–600.  
1029 doi:10.1007/s11214-017-0359-3.

1030 Harvey, V.L., Pedatella, N., Becker, E., Randall, C.E., 2022. Evaluation  
1031 of polar winter mesopause wind in WACCMX+DART. *J. Geophys. Res.*  
1032 *Atmos.* doi:10.1029/2022JD037063.

1033 Heale, C.J., Bossert, K., Vadas, S.L., 2022a. 3D numerical simulation of  
1034 secondary wave generation from mountain wave breaking over Europe. *J.*  
1035 *Geophys. Res. Atmos.* 127. doi:10.1029/2021JD035413.

1036 Heale, C.J., Inchin, P.A., Snively, J.B., 2022b. Primary versus secondary  
1037 gravity wave responses at F-region heights generated by a convective  
1038 source. *J. Geophys. Res. Atmos.* 127. doi:10.1029/2019JD031662.

1039 Hindley, N.P., Mitchell, N.J., Cobbett, N., Smith, A.K., Fritts, D.C.,  
1040 Janches, D., Wright, C.J., Moffat-Griffin, T., 2022. Radar observations  
1041 of winds, waves and tides in the mesosphere and lower thermosphere over  
1042 South Georgia Island (54°s, 36°w) and comparison to WACCM simula-  
1043 tions. *Atmos. Chem. Phys.* doi:10.5194/acp-2021-981.

1044 Hines, C.O., 1997. Doppler-spread parameterization of gravity-wave momen-  
1045 tum deposition in the middle atmosphere. part 1: Basic formulation. *J.*  
1046 *Atmos. Sol.-Terr. Phys.* 59, 371–386. doi:10.1016/S1364-6826(96)00079-X.

1047 Hoffmann, P., Becker, E., Singer, W., Placke, M., 2010. Seasonal variation  
1048 of mesospheric waves at northern middle and high latitudes. *J. Atmos.*  
1049 *Sol.-Terr. Phys.* 72, 1068–1079.

1050 Holton, J.R., 1983. The influence of gravity wave breaking on the general  
1051 circulation of the middle atmosphere. *J. Atmos. Sci.* 40, 2497–2507.

1052 Huba, J.D., Becker, E., Vadas, S.L., 2023. Simulation study of the 15 jan-  
1053 uary 2022 tonga event: Development of super equatorial plasma bubbles.  
1054 *Geophys. Res. Lett.* 50. doi:10.1029/2022GL101185.

1055 Immel, T.J., England, S.L., Mende, B., Heelis, R.A., Englert, C.R., Edel-  
1056 stein, J., Frey, H.U., Korpela, E.J., abd W. W. Craig, E.R.T., Harris, S.E.,  
1057 Bester, M., Bust, G.S., Crowley, G., Forbes, J.M., Gérard, J.C., Harlan-  
1058 der, J.M., Huba, J.D., Hubert, B., Kamalabadi, F., Makela, J.J., Maute,  
1059 A.I., Meier, R.R., Raftery, C., Rochus, P., Siegmund, O.H.W., Stephan,  
1060 A.W., Swenson, G.R., Frey, S., Hysell, D.L., Saito, A., Rider, K.A., Sirk,  
1061 M.M., 2018. The Ionospheric Connection Explorer Mission: Mission Goals  
1062 and Design. *Space Sci. Rev.* 214. doi:10.1007/s11214-017-0449-2.

1063 Karlsson, B., Becker, E., 2016. How does interhemispheric coupling con-  
1064 tribute to cool down the summer polar mesosphere? *J. Clim.* 29, 8807–  
1065 8821. doi:10.1175/JCLI-D-16-0231.1.

1066 Knobloch, S., Kaifler, B., Dörnbrack, A., Rapp, M., 2023. Horizontal  
1067 wavenumber spectra across the middle atmosphere from airborne lidar ob-  
1068 servations during the 2019 southern hemispheric SSW. *Geophys. Res. Lett.*  
1069 50. doi:10.1029/2023GL104357.

1070 Körnich, K., Becker, E., 2010. A simple model for the interhemispheric  
1071 coupling of the middle atmosphere circulation. *Adv. Space Res.* 45, 661–  
1072 668. doi:10.1016/j.asr.2009.11.001.

1073 Lindborg, E., 2006. The energy cascade in a strongly stratified fluid. *J. Fluid*  
1074 *Mech.* 550, 207–242.

1075 Lindzen, R.S., 1981. Turbulence and stress owing to gravity  
1076 wave and tidal breakdown. *J. Geophys. Res.* 86, 9707–9714.  
1077 doi:10.1029/JC086iC10p09707.



- 1078 Liu, H.L., Lauritzen, P.H., Vitt, F., 2024a. Impacts of gravity waves on  
1079 the thermospheric circulation and composition. *Geophys. Res. Lett.* 51.  
1080 doi:10.1029/2023GL107453.
- 1081 Liu, H.L., Lauritzen, P.H., Vitt, F., Goldhaber, S., 2024b. Assessment of  
1082 gravity waves from tropopause to thermosphere and ionosphere in high-  
1083 resolution WACCM-X simulations. *Journal of Advances in Modeling Earth*  
1084 *Systems* 16. doi:10.1029/2023MS004024.
- 1085 Liu, H.L., Marsh, D.R., She, C.Y., Wu, Q., Xu, J., 2009. Momentum bal-  
1086 ance and gravity wave forcing in the mesosphere and lower thermosphere.  
1087 *Geophys. Res. Lett.* 36. doi:10.1029/2009GL037252.
- 1088 Liu, H.L., McInerney, J.M., Santos, S., Lauritzen, P.H., Taylor, M.A.,  
1089 Pedatella, N.M., 2014. Gravity waves simulated by high-resolution  
1090 Whole Atmosphere Community Climate Model. *Geophys. Res. Lett.* 41.  
1091 doi:10.1002/2014GL062468.
- 1092 Liu, H.L., Wang, W., Huba, J.D., Lauritzen, P.H., Vitt, F., 2023. Atmo-  
1093 spheric and ionospheric responses to Hunga-Tonga volcano eruption simu-  
1094 lated by WACCM-X. *Geophys. Res. Lett.* 50. doi:10.1029/2023GL103682.
- 1095 Lübken, F.J., 1997. Seasonal variation of turbulent energy dissipation rates  
1096 at high latitudes as determined by in situ measurements of neutral density  
1097 fluctuations. *J. Geophys. Res.* 102, 13441–13456.
- 1098 McFarlane, N.A., 1987. The effect of orographically excited gravity wave  
1099 drag on the general circulation of the lower stratosphere and troposphere.  
1100 *J. Atmos. Sci.* 44, 1775–1800.
- 1101 McLandress, C., Ward, W.E., Fomichev, V.I., Semeniuk, K., Beagley,  
1102 S.R., McFarlane, N.A., Shepherd, T.G., 2006. Large-scale dynamics  
1103 of the mesosphere and lower thermosphere: An analysis using the ex-  
1104 tended Canadian Middle Atmosphere Model. *J. Geophys. Res.* 111.  
1105 doi:10.1029/2005JD006776.
- 1106 Medvedev, A.S., Klaassen, G.P., 2000. Parameterization of gravity wave  
1107 momentum deposition based on nonlinear wave interactions: Basic formu-  
1108 lation and sensitivity tests. *J. Atmos. Sol.-Terr. Phys.* 62, 1015–1033.

- 1109 Nayak, C., Yigit, E., 2019. Variation of small-scale gravity wave ac-  
 1110 tivity in the ionosphere during the major sudden stratospheric warm-  
 1111 ing event of 2009. *J. Geophys. Res. Space Physics* 124, 470–488.  
 1112 doi:10.1029/2018JA026048.
- 1113 Plougonven, R., Zhang, F., 2014. Internal gravity waves from atmospheric  
 1114 jets and fronts. *Rev. Geophys.* 52, 33–76. doi:10.1002/2012RG000419.
- 1115 Podglajen, A., Hertzog, A., Plougonven, R., Legras, B., 2016. La-  
 1116 grangian temperature and vertical velocity fluctuations due to gravity  
 1117 waves in the lower stratosphere. *Geophys. Res. Lett.* 43, 3543–3553.  
 1118 doi:10.1002/2016GL068148.
- 1119 Sato, K., Kohma, M., Tsutsumi, M., Sato, T., 2017. Frequency spectra and  
 1120 vertical profiles of wind fluctuations in the summer Antarctic mesosphere  
 1121 revealed by MST radar observations. *J. Geophys. Res. Atmos.* 122, 3–19.  
 1122 doi:10.1002/2016JD025834.
- 1123 Sato, K., Tantenno, S., Watanabe, S., Kawatani, Y., 2012. Gravity wave  
 1124 characteristics in the southern hemisphere revealed by a high-resolution  
 1125 middle-atmosphere general circulation model. *J. Atmos. Sci.* 69, 1378–  
 1126 1396. doi:10.1175/JAS-D-11-0101.1.
- 1127 Sato, K., Tsuchiya, C., Alexander, M.J., Hoffmann, L., 2016. Clima-  
 1128 tology and ENSO-related interannual variability of gravity waves in  
 1129 the Southern Hemisphere subtropical stratosphere revealed by high-  
 1130 resolution AIRS observations. *J. Geophys. Res. Atmos.* 121, 7622–7640.  
 1131 doi:10.1002/2015JD024462.
- 1132 Sato, K., Yoshiki, M., 2008. Gravity wave generation around the polar vortex  
 1133 in the stratosphere revealed by 3-hourly radiosonde observations at Syowa  
 1134 Station. *J. Atmos. Sci.* 65, 3719–3735. doi:10.1175/2008JAS2539.1.
- 1135 Schaefer-Rolffs, U., Becker, E., 2018. Scale-invariant formulation of momen-  
 1136 tum diffusion for high-resolution atmospheric circulation models. *Mon.*  
 1137 *Wea. Rev.* 146, 1045–1062. doi:10.1175/MWR-D-17-0216.1.
- 1138 Schaefer-Rolffs, U., Knöpfel, R., Becker, E., 2014. A scale invariance criterion  
 1139 for les parametrizations. *Meteorol. Z.* doi:10.1127/metz/2014/0623.

1140 Senf, F., Achatz, U., 2011. On the impact of middle-atmosphere thermal  
1141 tides on the propagation and dissipation of gravity waves. *J. Geophys.*  
1142 *Res.* 116. doi:10.1029/2011JD015794.

1143 Simmons, A.J., Burridge, D.M., 1981. An energy and angular momentum  
1144 conserving vertical finite-difference scheme and hybrid vertical coordinates.  
1145 *Mon. Wea. Rev.* 109, 758–766.

1146 Smith, A.K., 2012. Global dynamics of the MLT. *Surv. Geophys.* 33, 1177–  
1147 1230. doi:10.1007/s10712-012-9196-9.

1148 Smith, S.A., Fritts, D.C., VanZandt, T.E., 1987. Evidence for a saturated  
1149 spectrum of atmospheric gravity waves. *J. Atmos. Sci.* 44, 1401–1410.  
1150 doi:10.1175/JAS-D-15-0324.1.

1151 Themens, D.R., Watson, C., Žagar, N., Vasylyevych, S., Elvidge, S., McCaf-  
1152 frey, A., Prikryl, P., Reid, B., Wood, A., Jayachandran, P.T., 2022. Global  
1153 propagation of ionospheric disturbances associated with the 2022 Tonga  
1154 volcanic eruption. *Geophys. Res. Lett.* 49. doi:10.1029/2022GL098158.

1155 Torr, M.R., Richards, P.G., Torr, D.G., 1981. Solar EUV energy budget of the  
1156 thermosphere. *Adv. Space Res.* 1, 53–61. doi:10.1016/0273-1177(81)90417-  
1157 8.

1158 Vadas, S.L., 2007. Horizontal and vertical propagation and dissipation of  
1159 gravity waves in the thermosphere from lower atmospheric and thermo-  
1160 spheric sources. *J. Geophys. Res.* 112. doi:10.1029/2006JA011845.

1161 Vadas, S.L., 2013. Compressible f-plane solutions to body forces, heatings,  
1162 and coolings, and application to the primary and secondary gravity waves  
1163 generated by a deep convective plume. *J. Geophys. Res. Space Physics*  
1164 118, 2377–2397. doi:10.1002/jgra.50163.

1165 Vadas, S.L., Azeem, I., 2021. Concentric secondary gravity waves in the  
1166 thermosphere and ionosphere over the continental United States on 25-  
1167 26 March 2015 from deep convection. *J. Geophys. Res. Space Phys.*  
1168 doi:10.1029/2020JA028275.

1169 Vadas, S.L., Becker, E., 2018. Numerical modeling of the excitation, prop-  
1170 agation, and dissipation of primary and secondary gravity waves during

1171 wintertime at McMurdo station in the Antarctic. *J. Geophys. Res. Atmos.*  
1172 123, 9326–9369. doi:10.1029/2017JD027974.

1173 Vadas, S.L., Becker, E., 2019. Numerical modeling of the generation of  
1174 tertiary gravity waves in the mesosphere and thermosphere during strong  
1175 mountain wave events over the Southern Andes. *J. Geophys. Res. Space*  
1176 *Phys.* 124, 7687–7718. doi:10.1029/2019JA026694.

1177 Vadas, S.L., Becker, E., Bossert, K., Baumgarten, G., Hoffmann, L., Harvey,  
1178 V.L., 2023a. Secondary gravity waves from the stratospheric polar vor-  
1179 tex over ALOMAR observatory on 12-14 January 2016: Observations and  
1180 modeling. *J. Geophys. Res. Atmos.* 128. doi:10.1029/2022JD036985.

1181 Vadas, S.L., Becker, E., Bossert, K., Hozumi, Y., Stober, G., Harvey, V.L.,  
1182 Baumgarten, G., Hoffmann, L., 2024. The role of the polar vortex jet in the  
1183 generation of primary and higher-order gravity waves in the stratosphere,  
1184 mesosphere and thermosphere during 11-14 january 2016. *J. Geophys. Res.*  
1185 *Space Phys.* 129. doi:10.1029/2024JA032521.

1186 Vadas, S.L., Becker, E., Figueiredo, C.A.O.B., Bossert, K., Harding, B.J.,  
1187 Gasque, L.C., 2023b. Primary and secondary gravity waves and large-scale  
1188 wind changes generated by the Tonga volcanic eruption on 15 January  
1189 2022: Modeling and comparison with ICON-MIGHTI winds. *J. Geophys.*  
1190 *Res. Space Phys.* 128. doi:10.1029/2022JA031138.

1191 Vadas, S.L., Crowley, G., 2010. Sources of the traveling ionospheric  
1192 disturbances observed by the ionospheric TIDDBIT sounder near Wal-  
1193 lops Island on October 30, 2007. *J. Geophys. Res. Space Physics* 115.  
1194 doi:10.1029/2009JA015053.

1195 Vadas, S.L., Figueiredo, C.A.O.B., Becker, E., Huba, J.D., Themens, D.R.,  
1196 Hindley, N.P., Galkin, I., Bossert, K., 2023c. Traveling ionospheric distur-  
1197 bances induced by the secondary gravity waves from the tonga eruption  
1198 on 15 January 2022: Modeling with MESORAC/HIAMCM/SAMI3 and  
1199 comparison with GPS/TEC and ionosonde data. *J. Geophys. Res. Space*  
1200 *Phys.* 128. doi:10.1029/2023JA031408.

1201 Vadas, S.L., Fritts, D.C., 2001. Gravity wave radiation and mean responses  
1202 to local body forces in the atmosphere. *J. Atmos. Sci.* 58, 2249–2279.

1203 Vadas, S.L., Fritts, D.C., 2002. The importance of spatial variability in the  
1204 generation of secondary gravity waves from local body forces. *Geophys.*  
1205 *Res. Lett.* 29. doi:10.1029/2002GL015574.

1206 Vadas, S.L., Fritts, D.C., Alexander, M.J., 2003. Mechanisms for the gen-  
1207 eration of secondary waves in wave breaking regions. *J. Atmos. Sci.* 60,  
1208 194–214. doi:10.1175/1520-0469(2003)060<0194:MFTGOS>2.0.CO;2.

1209 Vadas, S.L., Liu, H.L., 2009. Generation of large-scale gravity waves and  
1210 neutral winds in the thermosphere from the dissipation of convectively  
1211 generated gravity waves. *J. Geophys. Res.* 114. doi:10.1029/2009JA014108.

1212 Vadas, S.L., Liu, H.L., 2013. Numerical modeling of the large-scale neutral  
1213 and plasma responses to the body forces created by the dissipation of  
1214 gravity waves from 6 h of deep convection in Brazil. *J. Geophys. Res.* 118,  
1215 2593–2617. doi:10.1002/jgra.50249.

1216 Vadas, S.L., Liu, H.L., Lieberman, R.S., 2014. Numerical modeling of  
1217 the global changes to the thermosphere and ionosphere from the dissi-  
1218 pation of gravity waves from deep convection. *J. Geophys. Res.* 119.  
1219 doi:10.1002/2014JA020280.

1220 Vadas, S.L., Zhao, J., Chu, X., Becker, E., 2018. The excitation of secondary  
1221 gravity waves from local body forces: Theory and observation. *J. Geophys.*  
1222 *Res. Atmos.* 123, 9296–9325. doi:10.1029/2017JD027970.

1223 Xu, S., Vadas, S.L., Yue, J., 2021. Thermospheric traveling atmospheric  
1224 disturbances in austral winter from GOCE and CHAMP. *J. Geophys.*  
1225 *Res. Space Phys.* 126. doi:10.1029/2021JA029335.

1226 Zhang, S.R., Vierinen, J., Aa, E., Goncharenko, L.P., Erickson, P., Rideout,  
1227 W., Coster1, A.J., Spicher, A., 2022. Tonga volcanic eruption induced  
1228 global propagation of ionospheric disturbances via Lamb waves. *Frontiers*  
1229 *in Astronomy and Space Sciences* 9. doi:10.3389/fspas.2022.871275.

1230 Zhao, J., Chu, X., Chen, C., Lu, X., Fong, W., Yu, Z., Jones, R.M., Roberts,  
1231 B.R., Dörnbrack, A., 2017. Lidar observations of stratospheric gravity  
1232 waves from 2011 to 2015 at McMurdo (77.84°S, 166.69°E), Antarctica:  
1233 1. Vertical wavelengths, periods, and frequency and vertical wavenumber  
1234 spectra. *J. Geophys. Res. Atmos.* 122. doi:10.1002/2016JD026368.